UNIVERSITEIT UTRECHT

MASTER THESIS

Chiral Magnetic Effect in Weyl Semimetals

Author:
Richard van DONGEN

Supervisor:
Prof. Henk STOOF

A thesis submitted in fulfillment of the requirements for the degree of Master of Science

in the

Institute for Theoretical Physics

December 19, 2016

Universiteit Utrecht

Abstract

Betawetenschappen
Institute for Theoretical Physics

Master of Science

Chiral Magnetic Effect in Weyl Semimetals

by Richard van DONGEN

0.1 Abstract

This research has been motivated by recent discoveries of new states of matter in solid state physics such as the Weyl semimetal. This semimetal hosts electrons that behave as massless Weyl fermions and has the unique ability to conduct an electric current in the same direction as the magnetic field by which it is induced. This is called the chiral magnetic effect and it is related to the chiral anomaly in quantum field theory.

In this thesis the conductivity of a Weyl semimetal due to the chiral magnetic effect is derived by using field-theoretical techniques. It was found that the renormalization procedure is ambiguous in the sense that it determines the conductivity of the chiral magnetic effect up to a constant. This constant is found to be different in a system with broken inversion symmetry than in a system with broken time reversal symmetry. It is also argued that no current can flow in the static limit when inversion symmetry is broken, from which this constant is determined. In accordance with previous research, an analytic function is obtained for the conductivity in the presence of a chemical and chiral potential at zero temperature when applying a magnetic field with a given frequency and wavenumber. It was found that the value of the conductivity is not well-defined in experiments in which the frequency and wavenumber of the applied magnetic field are zero. This is due to the fact that the value for the conductivity was found to depend on the ratio between these two quantities. For a full understanding of Weyl semimetals in a realistic environment, further research must be conducted to determine their behaviour at finite temperature and interactions between the Weyl fermions must be incorperated into future models.

Preface

Since the experimental discovery of the two-dimensional material graphene in 2004 the interest of the physics community in new states of solid matter has exploded. Graphene shows great possiblities for applications, because of its special properties, such as its immense strength and the ability to conduct electric current better than even copper. Another new state of solid matter was discovered in 2005, the topological insulator. This material is a mix of an insulator in the bulk and a conductor on its surface. The electronic surface states are symmetry protected, making them robust to perturbations on the surface. A great interest has been developed in the possible applications of these surface states in fields such as quantum computing. As late as 2015 yet another new type of material was discovered, the Weyl semimetal. This semimetal exhibits similar electronic states as the surface of topological insulators, but they are topologically protected, instead of symmetry protected. This feature makes them even more robust against perturbations. Furthermore, the material is able to conduct non-dissipative currents, making it a great candidate for radical improvements in different types of industry, as it does not produce any heat at all. The enormous burst of interest in topological materials, and in particular Weyl semimetals has motivated me to dedicate my thesis to investigate transport features of this new type of material.

In this thesis I start by giving an introduction on the nature of electronic transport in materials, starting from regular conductors, semiconductors and insulators, up to three-dimensional Weyl semimetals. Then follows an explanation of the topological nature of this material and the chiral magnetic effect. Then an experiment in which the chiral magnetic effect was observed is discussed. I state that the central result in this thesis poses a technical difficulty in this experiment. This discussion is followed by the derivation of the conductivity due to the chiral magnetic effect in Weyl semimetals at zero temperature. After presenting the results, I conclude with discussing this technical difficulty, along with another technicality that arises when comparing the theory with the experiment. The technicality is that materials that are intrinsically a Weyl semimetal behave differently in an experiment than a Dirac semimetal that is turned into a Weyl semimetal by breaking time reversal symmetry. The two materials behave differently because a different symmetry is broken in these materials.

I was engaged in writing this thesis from February to December 2016 at the university of Utrecht. I would like to thank my supervisor, Henk Stoof, for his excellent guidance and support during this period of time, along with his PhD student, Erik van der Wurff, who has taken the time to help me out various times. I would also like to thank my fellow physics students with whom I have discussed several problems and who helped me to gain new insights. Naturally, my thanks also go out to Vasileios Dimitripoulos, whose thesis I have based my research on.

I hope you enjoy the reading of this thesis.

Richard van Dongen

Utrecht, December 18, 2016

Contents

Chapter 1

Introduction

1.1 Classification of Solids

Solid materials can be divided in classes in various ways. We catergorize them by their ability to conduct an electric current. From low to high conductance, we make a distinction between insulators, semi-conductors and conductors. The difference between these classes lies in their electronic band structures, which dictates the possible states of electrons in a material. Henceforth, understanding the band structure of a material allows us to get insight into transport properties of its electrons, such as electric conductance. In this section we will learn about this relation between the electronic band structure and electric conductance for the three types of materials. To simplify matters we consider large, homogeneous systems, making it a valid assumption that the band structure is continuous and that the band structure is identical everywhere in the material. We also focus only on crystalline materials, with a periodic structure on the microscopic scale.

The idea of a band structure stems from the notion that electrons in a (crystalline) material are described by the rules of quantum mechanics. The eigenstates of electrons can be expressed as Bloch waves, which are solutions of the Schrödinger equation. Their energies are given by the eigenvalue of the Schrödinger equation as a function of their wavenumber. Depending on the microscopic structure of the materials, more than one Bloch wave may exist with the same wavenumber. Each Bloch wave corresponds to an electronic band of the material and has its own dispersion relation. The electrons tend to fill up the bands with lowest energy first, after which bands of higher energy will be filled. Two specific bands are of primary interest when investigating transport properties of materials, the valence band and the conduction band. These are the last non-empty band and the first empty band at a temperature of 0 K, respectively. The relative position of these bands governs the behaviour of free electrons in the material. As an example, the full electronic band structure of diamand is displayed in Fig. 1.1. It is important to understand that band structures are complex in general, like for the example. However, in this thesis we will zoom in on interesting points of the band structure, where we encounter only the valence band and the conduction band. This is a valid approximation for low-energy electrons.

The electrons in the valence band can be excited to the conduction band by thermal fluctuations or by the absorption of photons. An electron in the conduction band can also emit a photon and go to the valence band accoringly. Such a transition will only take place if the new state of the electron is allowed by the band structure and is not yet occupied. Hence, the presence of vacancies at energies close the valence band determine the ability of a material to conduct a current. The chance of finding an electron with energy ϵ at temperature T is described by the Fermi-Dirac

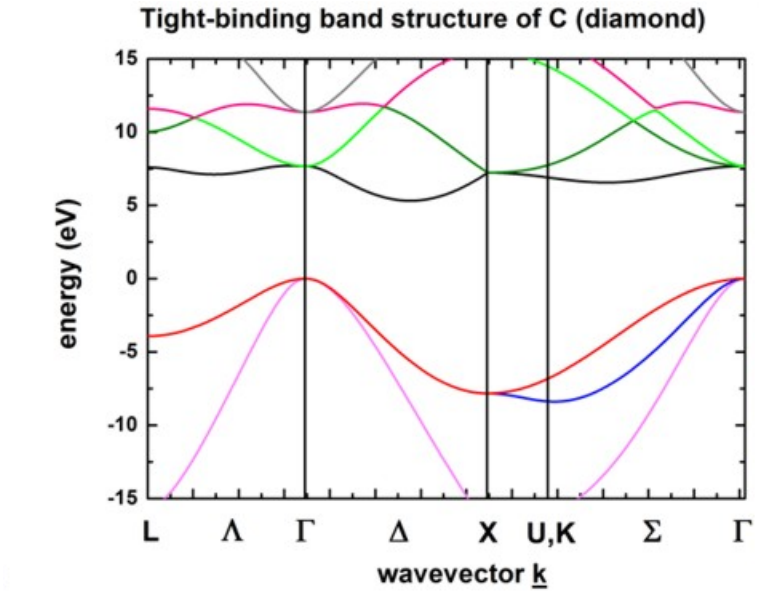

FIGURE 1.1: Dispersion relation of diamond. Every line denotes an electronic band. The symbols on the x-axis denote points in momentum space with symmetric properties. Adapted from Ref. [1].

distribution, $N_{FD}(\epsilon)$ and has the form

$$N_{FD}(\epsilon) = \frac{1}{e^{(\epsilon-\mu)/k_BT} + 1}, \tag{1.1}$$

where k_B is the Boltzmann constant and μ the chemical potential. The position of the chemical potential with respect to the valence band and conduction band are important for the electric properties of a material. Fig. 1.2 shows a schematic representation of the position of the chemical potential for each type of material. We see that for a metal and semimetal, together forming the group of conductors, the chemical potential lies inside the conductance band, while for a semiconductor and insulator the chemical potential lies between the bands. Electrons in a metal can easily be excited to a higher, vacant energy level and therefore metals are good conductors. In semimetals the number of allowed states is negligible at the chemical potential, but increases significantly around it. Excitation of electrons will happen less often than in a metal and the conductance will therefore not be as good as for a metal. However, semimetals still belong to the group of conductors, as they conduct currents relatively well. In semiconductors and insulators the electrons are not allowed to be excited to certain energies at all. There is a so called band gap between the valence band and the conduction band in which the chemical potential is located. Electrons with not enough energy to bridge this gap will not be exited, limiting the conductance. If the band gap is smaller than roughly the order of magnitude of the thermal energy k_BT, the material is considered to be a semiconductor, because the electrons can now occasionally be thermally excited. Thus a semiconductor does conduct electrical currents, albeit poorly in comparison to metals and semimetals. The chemical potential in semiconductors can be shifted by doping the material with impurities. Depending on the doping used, doped semiconductors end up as p-type or n-type semiconductors, having positive holes (of electrons) or negative electrons as current carriers, respectively. Doped semiconductors have different electrical properties than intrinsic semiconductors and they have their own

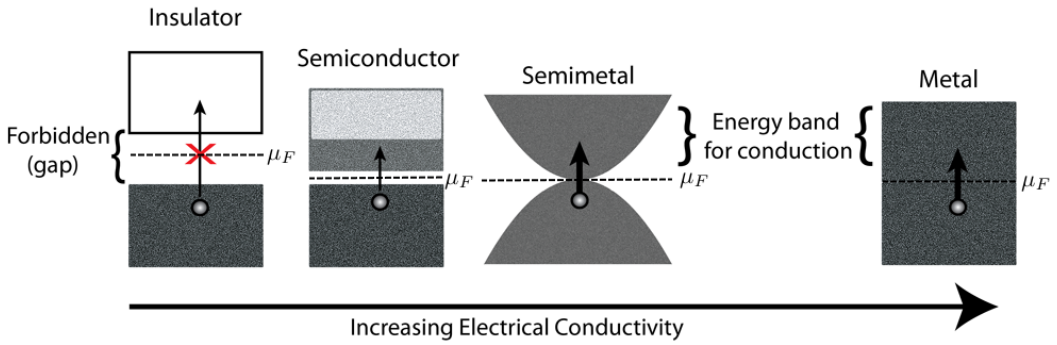

FIGURE 1.2: Schematic respresentation of the valence band and conduction band in an insulator, semiconductor, semimetal and conductor. The upper band are conduction bands and the lower bands are valence bands. For insulators and semiconductors the chemical potential, μ_F lies in the band gap between the valence band and conduction band. If the band gap is greater than roughly the order of magnitude of k_BT, the material is generally regarded as an insulator. The chemical potential in a semimetal lies on the touching point of the valence band and the conduction band and for a metal the chemical potential lies within the conduction band. Adapted from Ref. [2].

application in electronics. If the band gap of a material is greater than the order of magnitude of k_BT, it is considered to be an insulators and it practically does not conduct electric currents. For a more complete explanation of the electronic band structure and its implications, the reader can consult books, such as(Charles Kittel, Introduction to Solid State Physics).

1.2 Dirac Semimetals

The picture as drawn thus far shows the state of our understanding of solid materials as it was up until just a few years ago. In 2004 Novoselov et al. confirmed the existence of the two-dimensional material graphene for the first time [3]. Since then the material has been praised for its great electric and thermal conductivity, its immense strenght and many other convenient properties. These macroscopic properties can be understood by looking at the material on the microscopic scale, like we did in the previous section. Fig. 1.3 shows the microscopic structure of graphene, which consists of carbon atoms in a hexagonal lattice, which can be subdivided in sublattices A and B. Electrons can hop from one sublattices to the other. The dispersion relation of the electrons in graphene is shown in Fig. 1.4, where we see six different Dirac points, the touching points of the valence band and conduction band. However, due to symmetry we can subdivide these points in two groups of three equivalent points. The two unique points are denoted by K and K'. Around the Dirac points, we see that the dispersion relation can be approximated by so-called Dirac cones, that have a linear behaviour on the momenta. The Hamiltonian of such a Dirac cone is given by

$$H(\vec{k}) = \hbar v_F(\sigma^x k_x + \sigma^y k_y), \tag{1.2}$$

where $\hbar$ is the reduced Plank's constant, $\vec{k}$ the momentum vector with x-component k_x and y-component k_y, v_F the Fermi velocity and σ^i the i-th Pauli matrix. The Fermi velocity is typically of the order of 10^6 m/s [5]. The eigenenergies of this

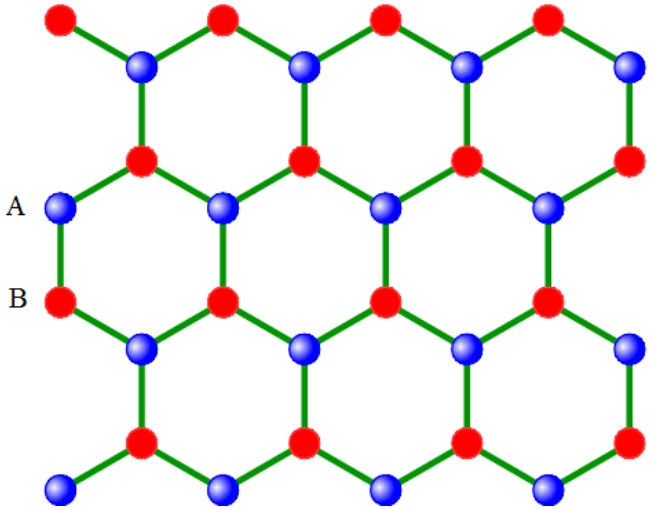

FIGURE 1.3: Microscopic structure of graphene. The red and blue dots represent carbon atom and the lines between them represent their bonds. The hexagonal structure can be subdivided in sublattices A and B, denoted by blue and red dots, respectively. Adapted from Ref. [4].

Hamiltonian are given by $E_\pm = \pm\hbar v_F k$, where k is the length of the momentum. Because of this semimetallic behaviour and its linear dispersion relation around the Dirac point, graphene is dubbed a two-dimensional Dirac semimetal.

It is possible to generalize the Hamiltonian of Eq. (1.2) to three dimensions to describe three-dimensional Dirac semimetals. The existence of these materials has been verified by experimental observations. An example of such material is Na_3Bi, which was discovered in 2014 [6]. The Hamiltonian of a three-dimensional Dirac semimetal reads

$$H(\vec{k}) = \hbar v_F \begin{pmatrix} \vec{\sigma}\cdot\vec{k} & 0 \\ 0 & -\vec{\sigma}\cdot\vec{k} \end{pmatrix}, \tag{1.3}$$

where $\vec{\sigma}$ denotes the three-dimensional vector of Pauli matrices. The two entries in the matrix correspond to electrons of different chirality. This is equal to ± 1, depending on the direction of the momentum with respect to the spin of the electron. The plus (minus) sign corresponds to a(n) (anti)parallel orientation. In this model there exist a chiral symmetry, which means that electrons of both chiralities behave the same. This is a direct result of the symmetries in the Hamiltonian. Let us therefore take a moment to inverstigate these symmetries. We claim that the Hamiltonian admits inversion symmetry and time reversal symmetry. Inversion send a momentum $\vec{k} \to -\vec{k}$ and time reversion sends both $\vec{k} \to$ and $\sigma \to -\sigma$. It is evident that the Hamiltonian is invariant under these transformations, as it gives back the same set of eigenstates with corresponding energies. Since it is symmetric in these operations, two electrons can occupy the same energy state and the Dirac point is occupied by four electrons. This means that the cones are two-fold degenerate and the Dirac point four-fold degenerate. This can be interpreted as two cones lying on top of each other. These cones are called Weyl cones.

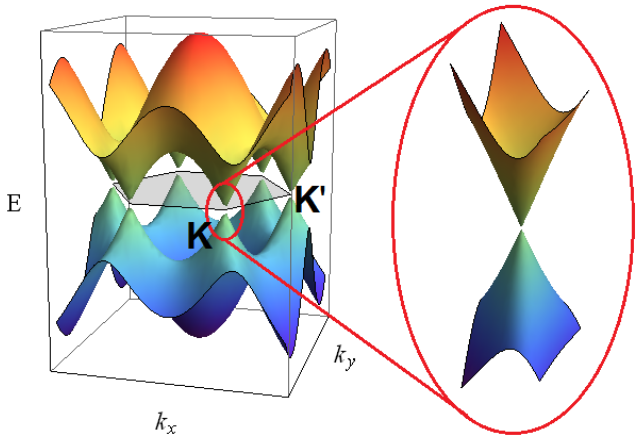

FIGURE 1.4: Dispersion relation of electrons in graphene. The horizontal axes shows the momenta of the electrons in the $x-$ and y-direction and the vertical axis shows their energy. Six touching points of the valence band and conduction band are shown, but only two of them are non-equivalent due to symmetry. These points are denoted by K and K'. Around the touching point the dispersion relation behaves linearly and can be approximated by a Dirac cone. Adapted from Ref. [7].

1.3 Three-dimensional Weyl Semimetals

New physics arises when inversion symmetry or time reversal symmetry in a Dirac semimetal is broken. Such a material is called a Weyl semimetal (WSM). The result of this symmetry breaking is shown in Fig. 1.5. When inversion symmetry is broken, the Weyl cones split up in energy and when time reversal symmetry is broken, they are seperated in momentum. Breaking of time reversal symmetry can be realized in experiments by applying a magnetic field, while inversion symmetry is a property of the lattice of material. This cannot be easily broken, but a material can have an intrinsically broken inversion symmetry. In experiments inversion symmetry is usually broken, so we will use the picture of a broken inversion symmetry in this thesis as well.

The Hamiltonian of one Weyl cone can be described by

$$H(\vec{k}) = \pm\hbar v_F \vec{k} \cdot \vec{\sigma}. \tag{1.4}$$

The sign corresponds to the chirality of the electrons again. We see from this Hamiltonian that perturbations of the material in any direction do not drastically change the form of the Hamiltonian. Such a perturbation will only shift the position of the cone in its momentum. Since this does not destroy the electronic states, we say that they are topoligical protected [9]. This amounts to a large stability of the electrons in a three-dimensional Weyl semimetal.

Before turning to the topological nature of WSMs we would like to mention the experimental discovery of a WSM in 2015 when experimental groups have observed Weyl fermions in a crystal of tantalum arsenide (TaAs), in which inversion symmetry was broken [10].

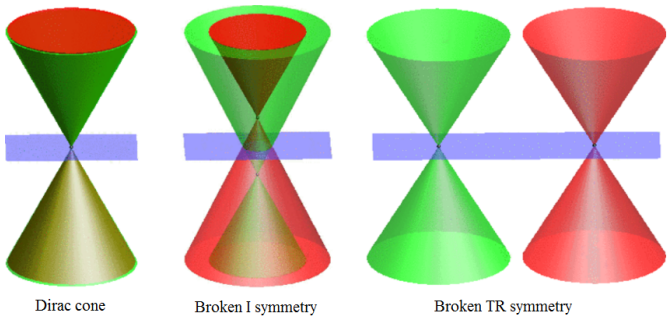

FIGURE 1.5: Symmetry breaking of a Dirac cone. The left picture shows a Dirac cone with both inversion and time reversal symmetry intact. The Dirac cone consists of two Weyl cones lying on top of each other. The middle picture shows the Weyl cones seperated in energy as a result of inversion symmetry breaking. In the right picture time reversal symmetry is broken and the Weyl cones are seperated in momentum. Adapted from Ref. [8].

1.4 Topology in Weyl semimetals

It must be clear by now that Weyl semimetals have nontrivial properties due to the form of their electronic band structure. The Weyl points play a crucial role in the unique properties of the material. These points are of topological nature. Therefore the topological nature of the Weyl points deserve a discussion. Although we try to be complete, we also have to be concise. Therefore the interested reader may consult Ref. [11] for a complete description.

Let us first elaborate shortly on some general topics in topology. Topology is a study in which one aims to ascribe properties, that are invariant to continuous deformations, of topological spaces. Allowed deformations are for example stretching and bending, while prohibited transformations are tearing and gluing of the space. Whenever a continuous transformations exists that deforms one space into another, the two spaces are topologically equivalent. Topologically equivalent spaces share common properties and theories on topologically equivalent spaces have a one-to-one connection, making it possible to define a theory on one space and deform it onto the other space.

The topology of a space can be determined with the use of topological invariants. These quantities depend only on the topology of the space and not on other details, such as its shape. One such quantity is the Euler characteristic, χ, which can be related to the Gaussian curvature, K. This is the product of the curvature of a surface in two orthogonal directions and depends on the position on the surface. However, if we integrate this Gaussian curvature over a whole surface, M, we obtain

$$\frac{1}{2\pi}\int_M K dA = 2 - 2g = \chi \tag{1.5}$$

where dA is the infinitessimal area of M and g is the genus of the object, which counts the number of holes in it. This shows that the Euler characteristic does not depend on the shape of the object, but only on its topology. Any object with the same number of holes in it has the same Euler characteristic. Fig. 1.6 shows a couple examples of the genera of different object. We see that whenever two objects have a completely different shape, they can still be topologically equivalent.

Now that we have become familiar with topology, we can turn to the task at

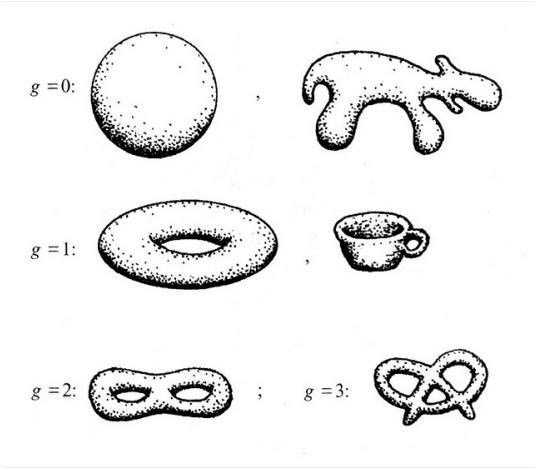

FIGURE 1.6: Various objects and their genera. Objects with the same genus are topologically equivalent and can thus be continuously deformation into one another. Adapted from Ref. [12].

hand, i.e. discussing the topological nature of WSMs. If WSMs can be described by their topological properties, a topological invariant must be attributed to it. This turns out to be determined by the so called Berry phase, which was introduced by Michael Berry in 1984 [11]. Before Berry's discovery, it was believed that whenever a quantum mechanical system would undergo a cyclic, adiabatic evolution, it would return to its original eigenstate without gaining an extra phase. In an adiabatic process the change is gradual enough for the system to adjust to it without leaving equilibrium. However, this does not cover the whole story as in some cases the eigenstate picks up an extra geometrical phase, called the Berry phase. The Berry phase, γ_n, is a topological quantity and is defined by

$$\gamma_n = i \oint_C d\vec{R} \langle n(\vec{R}) | \vec{\nabla}_{\vec{R}} | n(\vec{R}) \rangle, \tag{1.6}$$

where C is a closed curve, $|n(\vec{R})\rangle$ the eigenstate as a function of a vector of parameters , $\vec{R}$, on which the eigenstate depends and $\vec{\nabla}_{\vec{R}}$ is the gradient in parameter space. Since the eigenstates in a crystal can be decomposed in Bloch waves, we find that the only parameter is the wavenumber, k. Hence we might define the Berry phase as an integral in momentum space. Let us then redefine the Berry phase and write

$$\gamma_n = i \oint_C d\vec{k} \sum_n \langle u_{n,\vec{k}} | \vec{\nabla}_{\vec{k}} | u_{n,\vec{k}} \rangle = \oint_C d\vec{k} \cdot \vec{\mathcal{A}}(\vec{k}), \tag{1.7}$$

where $|u_{n,\vec{k}}\rangle$ is the eigenstate in the n-th band and $\vec{\mathcal{A}}(\vec{k}) = i \sum_n \langle u_{n,\vec{k}} | \vec{\nabla}_{\vec{k}} | u_{n,\vec{k}} \rangle$ is the Berry connection. Since the Berry phase is invariant under transformations of the form

$$\vec{\mathcal{A}}(\vec{k}) \to \vec{\mathcal{A}}(\vec{k}) + \vec{\nabla}_{\vec{k}} \beta(\vec{k}) \tag{1.8}$$

the field $\vec{\mathcal{A}}(\vec{k})$ shows a resemblance to the electromagnetic gauge field. Along with the Berry connection, we define the Berry curvature (sometimes referred to as Berry flux) as

$$\vec{B}(\vec{k}) = \vec{\nabla}_{\vec{k}} \times \vec{\mathcal{A}}(\vec{k}), \tag{1.9}$$

which shows similarities to the definition of the magnetic field in electrodynamics. Using Stokes' theorem we can rewrite Eq. (1.7) as

$$\gamma_n = \int_S \vec{B} \cdot d\vec{S}. \tag{1.10}$$

We know from Cauchy's theorem that an integral along a closed path can only be nonzero if it encloses a singular point. This is the Weyl point in momentum space and it turns out to create the Berry curvature, being either a source or a sink of it, corresponding to a Weyl point of positive or negative chirality, respectively.

To better understand the physical meaning of these quantities, let us apply the found formulas to the Hamiltonian we wrote down in Eq. (1.4). The eigenstates of this Hamiltonian are

$$|+\rangle = \begin{pmatrix} \cos\frac{\theta}{2}e^{-i\phi} \\ \sin\frac{\theta}{2} \end{pmatrix} \quad \text{and} \quad \begin{pmatrix} \sin\frac{\theta}{2}e^{-i\phi} \\ \cos\frac{\theta}{2} \end{pmatrix} \tag{1.11}$$

and have corresponding positive energies $E_{\pm}(\vec{k}) = \hbar v_f k$. Plugging in these eigenstates in the definitions of the Berry connection and Berry curvature, we obtain the Berry curvature

$$\vec{B}(\vec{k}) = \pm\frac{1}{2k^2}\hat{k}, \tag{1.12}$$

where $\hat{k}$ is the unit vector of the momentum. Because of its radial form and the similarities between the definition of the Berry curvature and the magnetic field, this solution has the form of a magnetic monopole or antimonopole in momentum space, depending on the chirality (sign). It turns out that the integral of the Berry flux over a closed surface, S, that encloses a Weyl point gives

$$\int_S \vec{B}(\vec{k}) \cdot d\vec{S} = \pm 2\pi \tag{1.13}$$

which is a measure of the number of Weyl point, multiplied by its chirality in units of 2π. As we have mentioned before, Weyl point cannot be destroyed by perturbations in the Hamiltonian, as it does not need symmetry to survive. However, two Weyl points at the same point in momentum space will annihilate each other, much like how an electric monopole (electron) and antimonopole (positron) annihilate each other when they meet. The Weyl points would combine into a Dirac point, which does not have any topological nature. Therefore we justify that inversion symmetry or time reversal symmetry must be broken to seperate the Weyl points in momentum space for a WSM to exist.

1.5 Introduction to the Chiral Magnetic Effect

After all this effort to introduce Weyl semimetals, one would expect this material to have some special properties that can show up in experiments. Luckily, there is such a property. This is its ability to conduct an electric current parallel to an applied magnetic field. This is called the Chiral Magnetic Effect (CME). This effect is only predicted in Dirac and Weyl semimetals and quark-gluon plasmas. It was first observed in the Dirac semimetal $ZrTe_5$ in 2014 [13]. The effect was also measured in two independent particle accelerators in a quark-gluon plasma [14].

The CME current induced by a magnetic field is of the form

$$\vec{j} = \sigma_{CME}\vec{B}, \tag{1.14}$$

with $\vec{j}$ the CME current, $\vec{B}$ the applied magnetic field and σ_{CME} the associated conductivity. We will aim to find an analytic expression for the latter in this thesis. It measures the ability of the WSM to conduct an electric current in the direction in which the magnetic field is applied. The conducivity is also known as the inverse of resistivity. It is worth noting that this CME current is non-dissipative of nature, as it is topologically protected. Realizing systems that are able to conduct currents of this nature has quite a big impact on how we use electronics in everyday life. Not only does it reduce the energy loss in electric wires to zero, it also reduces the heat produced by electric transport. The latter has been a highly limiting factor in building compact machines, such as telephones and (super)computers, but also in high-power machines. Furthermore, non-dissipative currents are much more fire resistant as wires will not melt due to dissipation.

It may be clear from the name of the CME and from the preceding discussions that the CME is made possible by the fact that the fermions in a WSM are chiral fermions. Chiral systems in quantum mechanics are drastically different from classical chiral systems by the chiral anomaly and this is exactly what drives the CME. Let us therefore discuss this difference and its implications briefly. A full discussion on the subject can be found in Refs. [15] and [16].

Let us consider a system that consists of chiral fermions. Classically, one would expect the current of both types of fermions to be conserved. Two linear combinations of these current can be defined, the so-called axial current j^μ_A and the vector current j^μ_V, which we identify as the usual current from electromagnetism. The currents have the form

$$\begin{aligned} j^\mu_V &= \bar{\psi}\gamma^\mu\psi \\ j^\mu_A &= \bar{\psi}\gamma^\mu\gamma^5\psi, \end{aligned} \tag{1.15}$$

where ψ and $\bar{\psi}$ are the fermionic spinor field and its conjugate, γ^μ denotes the gamma matrices and γ^5 is the fifth gamma matrix. The spinor fields can be decomposed as $\psi = (\psi_+, \psi_-)^\intercal$, where $\psi_{+/-}$ denotes the fermion field with positive/negative chirality and $\intercal$ denotes the transpose. Writing out Eq. (1.15) in terms of this decomposition yields

$$\begin{aligned} j^\mu_V &= j^\mu_+ + j^\mu_- \\ j^\mu_A &= j^\mu_+ - j^\mu_-, \end{aligned} \tag{1.16}$$

where j_+ and j_- are the currents of the fermions with positive and negative chirality, respectively. It is now obvious that the vector current is the current from electromagnetism, as it is the total current of fermions, where the axial current is the difference between the currents of the fermions with positive and negative chirality. As mentioned before, both currents would be conserved in a classical system and both the total number of fermions and the difference of the fermions of positive and negative chirality would be conserved. This can be translated to the fact that the number of positive and negative chiral fermions would be conserved, independently. However in a quantum system the best one can hope for is to conserve only one of the currents. The current from QED must still be conserved and therefore the conservation of the axial current cannot be satisfied. This means that the number positive and negative chiral fermions can change, as long as the total number of fermions remains constant. Hence, fermions of different chirality can be interchanged with one another.

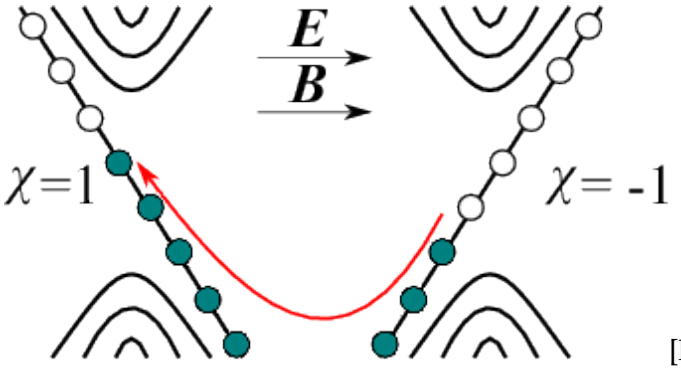

[h!]

FIGURE 1.7: Charge pumping between the right and left chiral cones, having chirality $\chi = 1$ and $\chi = -1$, respectively. The magnetic field rearranges the dispersion relations of both types of fermions in Landau levels. When an electric field is applied in the direction of the magnetic field, the fermions in the zeroth mode contribute to the pumping of right or left handed fermions to their opposite cones, depending on the sign of the electric field. In this case the electric field is parallel to the magnetic field and therefore the left handed fermions are pumped to the right handed cone. The particles are depicted by the grey circles and vacancies are white. This process causes an imbalance between the chiral fermions. Adapted from Ref. [17].

This way it is possible to create an imbalance between the two chiralities. The question now is how to realize this imbalance between chiral fermions in practise.
This can be understood by taking a look at how the conservation of the currents is not satisfied. For a suitable configuration of the electromagnetic field, this is captured by

$$\begin{aligned} \partial_\mu j^\mu_R &= \frac{e^2}{4\pi^2}\vec{E}\cdot\vec{B} \\ \partial_\mu j^\mu_L &= -\frac{e^2}{4\pi^2}\vec{E}\cdot\vec{B}, \end{aligned} \tag{1.17}$$

where we can clearly see that the loss of current in one chirality is gained in the other. It turns out that applying an electric and magnetic field that are not orthogonal to each other creates the imbalance in right and left chiral fermions. This can be explained by the fact that the magnetic field splits up the allowed energies in the Weyl cones in Landau levels, as depicted in Fig. 1.7. An electric field (anti)parallel to the magnetic field causes the fermions to move from the negative(positive) cone to the positive (negative) cone. This process is called charge pumping.

1.6 Experimental evidence of the chiral magnetic effect

The goal of every theoretical prediction is to be verified in experiments. This section is dedicated to an experimental observation that has been performed on the chiral magnetic effect. The results from this experiment will be discussed. Moreover, a short discussion is presented about the temperature-dependence in the experiments, which is interesting for our results, since we will investigate a model at temperature 0 K and for practical applications we need to understand the CME for finite temperatures. Furthermore we will discuss an ambiguity in the experiment, which we will try to fix in this thesis. We will discuss the observations of the CME in ZrTe5 [18].

This material is intrinsically a Dirac semimetal, but by applying an external magnetic field, time reversal symmetry is broken and the material behaves like a Weyl semimetal.

Eq. (1.14) shows the form of the CME current when a magnetic field is applied. The autors of the paper claim that

$$\vec{j}_{CME} = \frac{e^2}{2\pi^2}\Delta\mu\vec{B}, \tag{1.18}$$

where $\Delta\mu$ denotes the magnitude of the chiral imbalance. This result was obtained from Ref. [19]. In Section 1.5 we have given a way to produce a chiral imbalance in experiments. The description we used is however incomplete, as the imbalance undergoes an unrestrained growth and will never reach equilibrium. In this paper an extra process was added that inhibits this growth, i.e. a scattering process that changes the chirality of the fermions. We will only give a short sketch of the model used in this paper, refraining from giving much mathemetical detail. The interested reader can use the given references to study the subject in more depth. The chiral charge density in the used model is

$$\rho_A = \frac{\mu_A^3}{3\pi^2 v_F^3} + \frac{\mu_A}{3v_F^3}(T^2 + \frac{\mu^2}{\pi^2}), \tag{1.19}$$

where ρ_A is the chiral charge, μ_A the chiral imbalance, μ the chemical potential and T the temperature. The change in this chiral charge density is given by

$$\frac{\partial\rho_5}{\partial t} = \frac{e^2}{4\pi^2}\vec{E}\cdot\vec{B} - \frac{\rho_5}{\tau_V}, \tag{1.20}$$

where the first term drives the chiral charge pumping as we have seen in section 1.5 and the second term is the scattering effect, with τ_V the scattering time. After a time $t \gg \tau_V$ the system has found an equilibrium and after plugging in Eq. (1.19), one obtains the chiral chemical potential

$$\mu_5 = \frac{3}{4}\frac{v^3}{\pi^2}\frac{e^2}{\hbar^2 c}\frac{\vec{E}\cdot\vec{B}}{T^2 + \frac{\mu^2}{\pi^2}}\tau_V. \tag{1.21}$$

This chiral chemical potential can be substituted in Eq. (2.1) and one obtains, after redefining the temperature-dependent function $a(T)$

$$\vec{J}_{CME} = a(T)\left(\vec{E}\cdot\vec{B}\right)\vec{B}. \tag{1.22}$$

The paper defines the CME conductivity as

$$J^i_{CME} = a(T)B^iB^kE^k = \sigma^{ik}_{exp}E^k, \tag{1.23}$$

where we have given the conductivity a different subscript to distinguish it from the conductivity defined in Eq. (1.14). Also one should note that the value of σ^{ik}_{exp} is independent of its indices, so we will leave them out for the rest of the discussion. One finds that the CME conductivity has the form

$$\sigma_{exp} = a(T)B^2\cos\theta. \tag{1.24}$$

It is important to note the quadratic behaviour in the magnetic fields strength and the angular dependence θ between the electric and magnetic field. However, the chiral magnetic effect is not the only process in play. The electric field also produces an electric current through the material, so the total current has the form

$$J = J_{Ohm} + J_{CME} = (\sigma_{Ohm} + \sigma_{exp})E = \sigma_{tot}E, \tag{1.25}$$

where σ_{tot} is the total conductivity. The resistivity can be approximated by

$$\rho = \frac{1}{\sigma_{tot}} \approx \frac{1}{\sigma_{Ohm}} - a(T)B^2\cos\theta. \tag{1.26}$$

With this background we can take a look at the observations made by the team, which are shown in Fig. 1.8. The electric field was applied in the a-direction on the axis shown in the middle panel. The first panel shows the resistivity as function of the temperature for various magnetic field strengths when the magnetic and electric field are aligned. It exhibits a maximum at approximately 60 K. The location of the peak is thought to depend on the impurities of the sample and is not of any relevance for us. In the second panel we see the resistivity as function of the magnetic field strength for different angles, ϕ, between the magnetic and electric field. The angluar dependence is captured in Eq. (1.24), but one should notice that the angle ϕ from the figure and θ from the equation are different from each other in the sense that they are complementary angles. This has no physical relevance, but this is a result of the choice of definitions. In this graph the line at $90°$ has therefore no connection to the CME, because the electric and magnetic field are orthogonal. This displays the conventional restitivity of the material, which is a quadratic dependent on the magnetic field for low magnetic field strengths and experiences saturation at higher values. When increasing the angle, the contribution of the CME becomes increasingly important as the positive intrinsic resistivity is partially canceled out by the negative contribution of the CME resistivity. The data for $\phi = 90°$ is not well respresented in this plot and therefore the same data is shown in the last panel, but the vertical axis has been scaled logarithmically. The (negative) contribution from the CME is evidently clear in this figure.

Furthermore the team has investigated the temperature-dependence of the CME. The resistivity has been measured for various temperatures when the electric and magnetic field are aligned. This is shown in the left panel of Fig. 1.9. Recalling that the intrinsic resistivity of the material is positive and the CME contribution is negative, we see that the CME becomes of less relevance at greater temperatures. The right panel shows the measured resistivity (red lines) and its theoretical prediction and they match for the most part. However, the curve exhibits a minimum at zero magnetic field, where a peak is predicted to show up. The researchers do not have a definite explanation for this behaviour, but they suspect it might be caused by a small perpendicular contribution of the magnetic and electric field as a result of a small miss-alignment in the experiment. The inset in the right panel shows the temperature-dependent behaviour of the function $a(T)$ in Eq. (1.24). The function was shown to fall off faster than $1/T$ which is in accord with the temperature-dependence of Eq. (1.21) that dictates the behaviour of the CME conductivity with respect to temperature.

Eventhough this paper has presented evidence for the CME, something does not seem to be quite clear. Eq. (2.1) is used in this experiment to determine the magnitude of the chiral magnetic effect. This expression was calculated in Ref. [19] for the static limit. In the static limit the applied magnetic field is time-independent and this

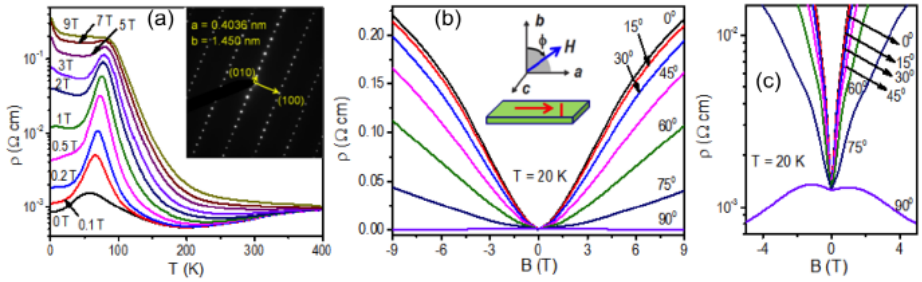

FIGURE 1.8: Measurements of the resistivity of ZrTe5 for as function of different parameters. The electric field is applied in the a direction as depicted in the inset in the second panel. (a) The Resistivity is plotted as a function of temperature for different strengths of the mangetic field, which is applied perpendicular to the cleavage plane of the crystal, as shown in the inset. The cleavage plane is the $a-c$ plane in the second panel and is shown in the inset. (b) Resistivity as function of the magnetic field strength for various angles ϕ between the electric and magnetic field at temperature $T = 20$K. (c) The same data as in the second panel, but with a logarithmic scale on the verical axis to emphasize the behaviour at $\phi = 90°$, where the CME is optimal. Adapted from Ref. [18].

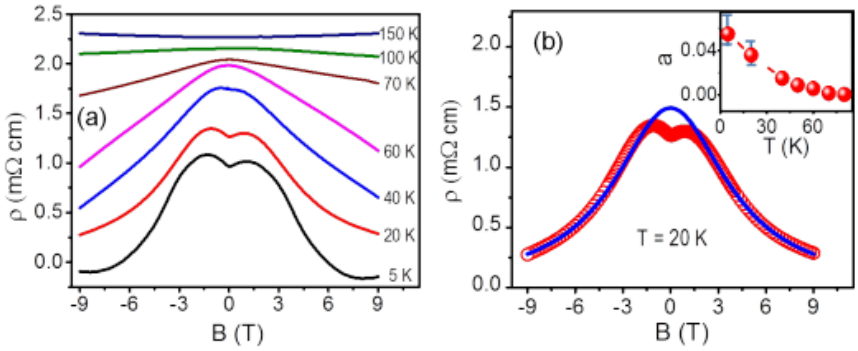

FIGURE 1.9: (a) Resistivity as function of the magnetic field strength for various temperatures ranging from 5 K to 150 K. The curves have been shifted by 1.5mΩcm (150 K), 0.9mΩcm (100 K), 0.2mΩcm (70 K and 5K). (b) Experimental value of the resistivity at 20 K for parallel electric and magnetic field (red line) and the theoretical prediction for the CME resistivity (blue line). The inset shows the temerature-dependence of the proportionality function $a(T)$ in units of S/(cm T^2). Adapted from Ref. [18].

is exactly the case in the experiment. However, the magnetic field was also uniform, which corresponds to the uniform limit. The central result in this thesis shows that both limits behave differently, even when they are combined and the magnetic field is time-independent and uniform. This raises the question if the choice of the static limit in this experiment is justified. This question will be answered in this thesis.

Now that we have established a solid understanding of the connection between macroscopic and microscopic properties of materials, the nature of the WSM and CME, it is time to conclude the introduction and commence the calculation of the CME conductivity.

Chapter 2

The Chiral Magnetic Effect

2.1 Linear Response Theory

In quantum physics it is important to acquire measurable, physical properties of the system under investigation from the somewhat abstract quantum mechanical quantities. This section aims to do exactly that by finding a way to relate the applied magnetic field to the expectation value of the electric current flowing through the WSM. For this purpose we apply linear response theory, which gives a valid approximation for calculating small fluctuations of physical quantities about their average values when small (electromagnetic) fields are applied. We will mainly follow the line of thought of Ref. [20] throughout the derivation.

The general idea of linear response theory is to apply a small perturbation to the system at some position $\vec{x}'$ and time t' and determine its response at position $\vec{x}$ and time $t > t'$. One should note that $t > t'$ must hold in order to satisfy causality. The quantity we would like to calculate is

$$\langle j^{\mu}\left(\vec{x},t\right)\rangle = \langle \bar{\psi}\left(\vec{x},t\right)\gamma^{\mu}\psi\left(\vec{x},t\right)\rangle, \tag{2.1}$$

which is the current of quantum electrodynamics, which is conserved by the symmetry of the theory. This current couples to the electromagnetic gauge field with coupling constant e, which we know as the electron charge. The total Hamiltonian for the fermions, H_T, can be expressed as

$$H_T\left(t\right) = H\left(t\right) + H_{int}\left(t\right) = H\left(t\right) + e\int d^3x' j^{\mu}\left(\vec{x}',t\right)A_{\mu}\left(\vec{x}',t\right), \tag{2.2}$$

with $A_{\mu}\left(\vec{x},t\right)$ the electromagnetic gauge field and $H_{int}\left(t\right)$ the interacting part of the Hamiltonian. Since we consider fluctuations around the equilibrium of the unperturbed system, the expectation value of the current can be expressed as

$$\langle j^{\mu}\left(\vec{x},t\right)\rangle = \langle G|j^{\mu}\left(\vec{x},t\right)|G\rangle, \tag{2.3}$$

with $|G\rangle$ the ground state of H. In the Heisenberg picture, where the time-dependence is captured inside the operators, the perturbation of the Hamiltonian will result in the redefinition $j^{\mu}\left(\vec{x},t\right) = U^{-1}\left(t\right)j^{\mu}\left(\vec{x},t\right)U\left(t\right)$. $U\left(t\right)$ is the unitary time evolution operator, defined as

$$U\left(t\right) = e^{-\frac{i}{\hbar}\int_{-\infty}^{t}dt' H_{int}(t')}. \tag{2.4}$$

For small perturbations Eq. (2.1) can be expanded as

$$\begin{aligned}\langle j^{\mu}(\vec{x},t)\rangle &= \langle G|e^{\frac{i}{\hbar}\int_{-\infty}^{t}dt' H_{int}(t')} j^{\mu}(\vec{x},t)\, e^{-\frac{i}{\hbar}\int_{-\infty}^{t}dt' H_{int}(t')}|G\rangle \\ &\approx \langle G|j^{\mu}(\vec{x},t)\,|G\rangle + \frac{i}{\hbar}\int_{-\infty}^{t}\langle G|\left[H_{int}\left(t'\right), j^{\mu}(\vec{x},t)\right]|G\rangle \\ &= \langle G|j^{\mu}(\vec{x},t)\,|G\rangle + \delta\langle G|j^{\mu}(\vec{x},t)\,|G\rangle.\end{aligned} \tag{2.5}$$

For the free fermion theory there is no reason for a net current to flow in any direction, so we can safely set the first term in Eq. (2.5) to zero and we see that the expectation value of the current will be equal to only the linear response to the perturbation. Writing out the interaction Hamiltonian as in Eq. (2.2) gives us a grasp of what the response will look like.

$$\begin{aligned}\langle j^{\mu}(\vec{x},t)\rangle &= -\frac{i}{\hbar}\int_{-\infty}^{t}dt'\int d^3x'\langle G|\left[j^{\mu}(\vec{x},t), j^{\nu}\left(\vec{x}',t'\right)\right]|G\rangle A_{\nu}\left(\vec{x}',t'\right) \\ &= \int_{-\infty}^{t}dt'\int d^3x'\chi^{\mu\nu}\left(\vec{x},t;\vec{x}',t'\right)A_{\nu}\left(\vec{x}',t'\right) \quad ,\end{aligned} \tag{2.6}$$

with

$$\chi^{\mu\nu}\left(\vec{x},t;\vec{x}',t'\right) = \frac{-i}{\hbar}\theta\left(t-t'\right)\langle G|\left[j^{\mu}(\vec{x},t), j^{\nu}\left(\vec{x}',t'\right)\right]|G\rangle \tag{2.7}$$

defined as the WSM's susceptibility to electromagnetic fields. Please note that the Heaviside step function, $\theta\left(t-t'\right)$ is included in order to define it in the general case, where t and t' are not yet defined. The electromagnetic susceptibility of a material is something we can actually measure! However, it is still not very practical to measure the susceptibility in the form of Eq. (2.7). We will therefore Fourier transform the susceptibility in both the temporal and spatial variables, as it is more convenient to measure the response of a material for an electromagnetic field with a specific frequency and wavenumber. We start with a transformation in the temporal coordinates by writing

$$A_{\mu}(\vec{x},t) = \int_{-\infty}^{\infty}\frac{d\omega}{2\pi}e^{-i\omega t}A_{\mu}(\omega,\vec{x})\,. \tag{2.8}$$

We plug this into Eq. (2.6) to obtain

$$\begin{aligned}\langle j^{\mu}(\vec{x},t)\rangle &= -\frac{i}{\hbar}\int_{-\infty}^{\infty}\frac{d\omega}{2\pi}e^{i\omega t}\int d^3x'\int_{-\infty}^{t}dt' e^{-i\omega(t'-t)}\chi^{\mu\nu}\left(\vec{x},t;\vec{x}',t'\right)A_{\nu}\left(\omega,\vec{x}'\right) \\ &= -\frac{i}{\hbar}\int_{-\infty}^{\infty}\frac{d\omega}{2\pi}e^{-i\omega t}\int d^3x'\int_{-\infty}^{0}dt' e^{-i\omega t'}\chi^{\mu\nu}\left(\vec{x},t;\vec{x},t'+t\right)A_{\nu}\left(\omega,\vec{x}'\right) \quad ,\end{aligned} \tag{2.9}$$

where we used the identity $e^{-i\omega t}e^{-i\omega(t'-t)} = e^{i\omega t'}$ in the first line. Furthermore, we may claim that the time dependence of the electromagnetic susceptibility is only proportional to $t-t'$, since it only depends on the time difference between the the moment of perturbation and the moment of measurement. The system must be only invariant under time translation under which this difference is preserved. We can therefore write Eq. (2.6) as

$$\begin{aligned}\langle j^{\mu}(\vec{x},t)\rangle &= \int d^3x'\int_{-\infty}^{t}dt'\chi^{\mu\nu}\left(\vec{x},\vec{x'};t-t'\right)A_{\nu}\left(\vec{x}',t'\right) \\ &= \int d^3x'\chi^{\mu\nu}\left(\vec{x},\vec{x}',t\right) * A_{\nu}\left(\vec{x}',t\right) \quad ,\end{aligned} \tag{2.10}$$

in which the asterisk denotes the convolution operator. We can now use the convolution theorem to find

$$\langle j^{\mu}\left(\vec{x},t\right)\rangle = \int_{-\infty}^{\infty}\frac{d\omega}{2\pi}e^{-i\omega t}\int d^{3}x'\chi^{\mu\nu}\left(\omega;\vec{x},\vec{x}'\right)A_{\nu}\left(\omega,\vec{x}'\right) \tag{2.11}$$

Comparing Eq. (2.9) with Eq. (2.11) shows us that

$$\begin{aligned}\chi^{\mu\nu}\left(\omega;\vec{x},\vec{x}'\right) &= -\frac{i}{\hbar}\int_{-\infty}^{0}dt'e^{-i\omega t'}\langle G|\left[j^{\mu}\left(\vec{x},t\right),j^{\nu}\left(\vec{x}',t+t'\right)\right]|G\rangle \\ &= -\frac{i}{\hbar}\int_{-\infty}^{0}dt'e^{-i\omega t'}\langle G|\left[j^{\mu}\left(\vec{x},0\right),j^{\nu}\left(\vec{x}',t'\right)\right]|G\rangle,\end{aligned} \tag{2.12}$$

where in the last line we used the fact that the susceptibility is invariant under time translation that preserve the time difference between the applied perturbation and the moment of measurement, as mentioned earlier.

For the spatial Fourier transformation we can follow precisely the same steps, since the electromagnetic susceptibility must only be invariant to spatial translation that preserve $\vec{x}-\vec{x}'$. The spatial Fourier transformation of the electromagnetic gauge field is

$$A_{\mu}(\vec{x},\omega) = \int\frac{d^{3}q}{\left(2\pi\right)^{3}}e^{i\vec{q}\cdot\vec{x}}A_{\mu}(\omega,\vec{q}) \tag{2.13}$$

and Eq. (2.11) becomes

$$\begin{aligned}&\langle j^{\mu}\left(\vec{x},t\right)\rangle = -\frac{i}{\hbar}\int_{-\infty}^{\infty}\frac{d\omega}{2\pi}e^{-i\omega t}\int\frac{d^{3}\vec{q}}{\left(2\pi\right)^{3}}e^{i\vec{q}\cdot\vec{x}}\int d^{3}x'e^{i\vec{q}\cdot\left(\vec{x'}-\vec{x}\right)} \\ &\times\langle G|\left[j^{\mu}\left(\omega,\vec{x}\right),j^{\nu}\left(\omega,\vec{x}'\right)\right]|G\rangle A_{\nu}\left(\omega,\vec{q}\right) \\ &= -\frac{i}{\hbar}\int_{-\infty}^{\infty}\frac{d\omega}{2\pi}e^{-i\omega t}\int\frac{d^{3}\vec{q}}{\left(2\pi\right)^{3}}e^{i\vec{q}\cdot\vec{x}}\int d^{3}x'e^{i\vec{q}\cdot\vec{x}'} \\ &\times\langle G|\left[j^{\mu}\left(\omega,\vec{x}\right),j^{\nu}\left(\omega,\vec{x}'+\vec{x}\right)\right]|G\rangle A_{\nu}\left(\omega,\vec{q}\right)\end{aligned} \tag{2.14}$$

Using the convolution theorem again, we find

$$\begin{aligned}\langle j^{\mu}\left(\vec{x},t\right)\rangle &= \int_{-\infty}^{\infty}\frac{d\omega}{2\pi}e^{-i\omega t}\int d^{3}x'\chi^{\mu\nu}\left(\omega,\vec{x}-\vec{x}'\right)A_{\nu}(\omega,\vec{x}') \\ &= \int_{-\infty}^{\infty}\frac{d\omega}{2\pi}e^{-i\omega t}\chi^{\mu\nu}\left(\omega,x\right)*A_{\nu}\left(\omega,\vec{x}\right) \\ &= \int_{-\infty}^{\infty}\frac{d\omega}{2\pi}e^{-i\omega t}\int\frac{d^{3}q}{\left(2\pi\right)^{3}}e^{i\vec{q}\cdot\vec{x}}\chi^{\mu\nu}\left(\omega,\vec{q}\right)A_{\nu}\left(\omega,\vec{q}\right)\end{aligned} \tag{2.15}$$

and combining Eqns. (2.14) and (2.15) yields

$$\begin{aligned}\chi^{\mu\nu}\left(q,\omega\right) &= -\frac{i}{\hbar}\int_{\infty}^{0}dt'e^{-i\omega t'}\int d^{3}x'e^{i\vec{q}\cdot\vec{x}'}\langle G|\left[j^{\mu}\left(\vec{x},0\right),j^{\nu}\left(\vec{x}',t+t'\right)\right]|G\rangle \\ &= -\frac{i}{\hbar}\int_{\infty}^{0}dt'e^{-i\omega t'}\int d^{3}x'e^{i\vec{q}\cdot\vec{x}'}\langle G|\left[j^{\mu}\left(0,0\right),j^{\nu}\left(\vec{x}',t'\right)\right]|G\rangle.\end{aligned} \tag{2.16}$$

Now that we have found the Fourier transform of the electromagnetic susceptibility, there is one problem left to solve. Namely, we are interested in the case in which a magnetic field is applied to the WSM and up till now we have applied an arbitrary electromagnetic field, $A_{\mu}\left(\omega,\vec{q}\right)$. Let us assume that the magnetic field is

applied in the x-direction. This choice may always be made, as the system is rotationally invariant. The magnetic field is related to the gauge field by

$$B_i\left(\omega,\vec{q}\right)=i\epsilon_{ijk}q_jA_k\left(\omega,\vec{q}\right), \tag{2.17}$$

where ϵ_{ijk} is the complete anti-symmetric symbol with $\epsilon_{123}=1$. We still have one unfixed gauge degree of freedom. By choosing a suitable gauge fixing, the magnetic field can be expressed as

$$B_x\left(\omega,\vec{q}\right)=-iq_zA_y\left(\omega,\vec{q}\right). \tag{2.18}$$

We can eventually write the Fourier transform of the expectation value of the electric current as

$$\left\langle j^x\left(\omega,\vec{q}\right)\right\rangle=\frac{i}{q_z}\chi^{xy}\left(\omega,\vec{q}\right)B_x\left(\omega,\vec{q}\right)=\sigma^x_{CME}\left(\omega,\vec{q}\right)B_x\left(\omega,\vec{q}\right), \tag{2.19}$$

where $\sigma^x_{CME}\left(\omega,\vec{q}\right)$ is the CME conductivity, as a function of the frequency ω and momentum $\vec{q}$ of the applied magnetic field. The conductivity is a measure of the material's ability to conduct an electric current, whereas its real part is the conductivity of a DC current and the imaginary part of an AC current. We thus aim to find an expression for

$$\sigma^x_{CME}\left(\omega,\vec{q}\right)=\frac{i}{q_z}\chi^{xy}\left(\omega,\vec{q}\right)=\frac{i}{q_z}\Pi^{xy}\left(\omega,\vec{q}\right), \tag{2.20}$$

where we identify $\chi^{\mu\nu}\left(\omega,\vec{q}\right)$ as the vacuum polarization diagram and call it $\Pi^{\mu\nu}\left(\omega,\vec{q}\right)$.

2.2 Green's function

In this section we calculate the Green's functions (also referred to as propagators) of the positive and negative chiral fermions from their free Lagrangian. Before going directly to the calculation, we first define the conventions we use throughout the thesis. We fix the reduced Planck's constant and the Fermi velocity by $\hbar = 1$ and $c = 1$. The metric is defined by $\eta^{\mu\nu} = (-1, 1, 1, 1)$ and the gamma-matrices are expressed in the Weyl basis. This is defined by $\{\gamma^\mu, \gamma^\nu\} = 2\eta^{\mu\nu}$. Explicitly this reads

$$\gamma^\mu = \left(\begin{pmatrix} 0 & -\mathbb{I} \\ \mathbb{I} & 0 \end{pmatrix}, \begin{pmatrix} 0 & \sigma^i \\ \sigma^i & 0 \end{pmatrix} \right), \quad \gamma^5 = \begin{pmatrix} \mathbb{I} & 0 \\ 0 & -\mathbb{I} \end{pmatrix}, \tag{2.21}$$

and

$$\mathbb{I} = \begin{pmatrix} 1 & 0 \\ 0 & 1 \end{pmatrix}, \quad \sigma^1 = \begin{pmatrix} 0 & 1 \\ 1 & 0 \end{pmatrix}, \quad \sigma^2 = \begin{pmatrix} 0 & -i \\ i & 0 \end{pmatrix}, \quad \sigma^3 = \begin{pmatrix} 1 & 0 \\ 0 & -1 \end{pmatrix}. \tag{2.22}$$

The free Lagrangian we start from is

$$\mathcal{L} = \bar{\psi} \left(-i\partial\!\!\!/ - \mu\gamma^0 + \mu_5\gamma^0\gamma^5 \right) \psi. \tag{2.23}$$

This massless Dirac Lagrangian contains a chemical potential μ, accompanied by a shift in energy of magnitude $\pm b_0$ for fermions with positive and negative chirality, respectively. The fermion field ψ is represented in Weyl spinors, i.e. $\psi = (\psi_+, \psi_-)^\intercal$, such that ψ_+ has positive chirality and ψ_- negative chirality. The two types of fermions will be described by different Green's functions due to the anti-symmetry in the chiralities.

As a first step, let us go to momentum space by writing

$$\psi(x^\mu) = \int \frac{d^4k}{(2\pi)^4} \tilde{\psi}(k^\mu) e^{ik\cdot x}, \quad \bar{\psi}(x^\mu) = \int \frac{d^4k}{(2\pi)^4} \tilde{\bar{\psi}}(k^\mu) e^{-ik\cdot x}. \tag{2.24}$$

We will drop the tilde on the ψ's from now on, as we will not go back to real space. The action can now be written as

$$S = \int \frac{d^4k}{(2\pi)^4} \bar{\psi}(k^\mu) \left(k\!\!\!/ - \mu\gamma^0 + \mu_5\gamma^0\gamma^5 \right) \psi(k^\mu). \tag{2.25}$$

The inverse Green's function is defined by

$$S = \int \frac{d^4k}{(2\pi)^4} \bar{\psi}(k^\mu) G^{-1}(k^\mu) \psi(k^\mu). \tag{2.26}$$

However, we will use a slightly different definition in accord with the literature, such that

$$\tilde{G}^{-1}(k^\mu) = \gamma^0 G^{-1}(k^\mu) = \gamma^0 \left(k\!\!\!/ - \mu\gamma^0 + \mu_5\gamma^0\gamma^5 \right). \tag{2.27}$$

Again, we will drop the tilde. Inverting $G^{-1}(k^\mu)$ yields the Green's function. This can easily be done by writing $G^{-1}(k^\mu)$ out explicitly. We define the effective chemical potential as $\mu_\pm \equiv \mu \mp \mu_5$ for positive and negative chirality. The explicit form of the

inverse Green's function becomes

$$G^{-1}(k^\mu) = \begin{pmatrix} -(k_0-\mu_+)\,\mathbb{I} - k\cdot\sigma & 0 \\ 0 & -(k_0-\mu_-)\,\mathbb{I} + k\cdot\sigma \end{pmatrix} = \begin{pmatrix} G^+(k^\mu)^{-1}+ & 0 \\ 0 & G^-(k^\mu)^{-1} \end{pmatrix}, \tag{2.28}$$

where $G^+(k^\mu)$ and $G^-(k^\mu)$ are the propagators for the fermions with positive and negative chirality, respectively. These matrices can easily be inverted separately, yielding

$$G^\pm(k^\mu) = \frac{-(k_0-\mu_\pm) \pm k\cdot\sigma}{(k_0-\mu_\pm)^2 - |\vec{k}|^2}. \tag{2.29}$$

It turns out to be convenient to decompose the propagators into the Dirac basis by writing

$$G^\pm(k^\mu) = \mathcal{G}_\mu(k^\mu)^\pm \sigma^\mu, \quad \text{with } \sigma^\mu = \left(\mathbb{I}, \sigma^i\right). \tag{2.30}$$

The coefficients read

$$\mathcal{G}_0^\pm(k^\mu) = -\frac{k_0-\mu_\pm}{(k_0-\mu_\pm)^2 - |\vec{k}|^2}, \quad \mathcal{G}_i^\pm(k^\mu) = \pm\frac{k_i}{(k_0-\mu_\pm)^2 - |\vec{k}|^2}. \tag{2.31}$$

It is worth noting that the denominators of the propagators of the positive and negative chiral electrons give rise to particles that live in the Weyl cones, as we have defined in the previous chapter. Using $k_0 = -\omega$, where ω is the frequency of the particle, we find a pole at

$$\omega_\alpha = \pm k - \mu_\alpha \tag{2.32}$$

for a particle with chirality $\alpha = \pm 1$. This indeed describes two Weyl cones that are split up in energy.

With this explicit form of the free propagators, we are fully equipped to perform calculations on interacting fermions.

2.3 CME Conductivity

In this section we are interested in calculating the conductivity due to the chiral magnetic effect (CME). The CME conductivity in momentum space is expressed by the Kubo formula as

$$\sigma^x_{CME}(\vec{q},\omega,\mu_+,\mu_-) = \frac{i}{q}\Pi^{xy}(\vec{q},\omega,\mu_+,\mu_-), \tag{2.33}$$

which is equivalent to Eq. (2.20), but with a different set of parameters and q_z has been replaced by q, the length of $\vec{q}$. Hence, $\vec{q}$ is chosen to be directed entirely in the $z-direction$. This is justified by the rotational symmetry of the system.

To describe the interactions of the fermions with the electromagnetic field, we add a coupling to the Lagrangian from Eq. (2.23). This reads

$$\mathcal{L} = \bar{\psi}\left(-i\partial\!\!\!/ - \mu\gamma^0 + \mu_5\gamma^0\gamma^5\right)\psi + e\bar{\psi}\gamma^\mu A_\mu\psi, \tag{2.34}$$

where e is the electronic charge. This is the Lagrangian from which the vacuum polarization diagram is calculated. A schematic representation for the diagram is shown in Fig. 2.1. The incoming and outgoing photon carry momentum $\vec{q}$ and the electrons have momentum $\vec{k}$ and $\vec{k}+\vec{q}$. The vacuum polarization follows from plug-

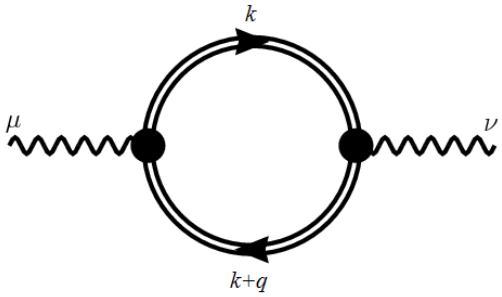

FIGURE 2.1: Vacuum polarization diagram in which the photon splits up into an electron and positron of equal chirality and later recombines to form a photon again. The electron propagators are shifted in energy as described in Eq. (2.28). The momentum of the incoming photon is $\vec{q}$, so that one electron carries momentum $\vec{k}$ and the other has $\vec{k}+\vec{q}$. Adapted from Ref. [21].

ging the vector current from Eq. (1.15) into Eq. (2.16) and performing the Fourier transform. We obtain

$$\Pi^{\mu\nu}(q) = e^2 \int \frac{d^4k}{(2\pi)^4} \operatorname{Tr}[G(k)\gamma^0\gamma^\mu G(k+q)\gamma^0\gamma^\nu]. \tag{2.35}$$

One should note that the extra terms γ^0 are added to be consistent with the choice of definition in Eq. (2.27). We will first determine the trace in this expression and then perform the integral explicitly.

Since we are interested in the xy-component of the vacuum polarization, we should consider the trace (dropping the arguments of the G's for a moment)

$$\operatorname{Tr}[G\sigma^\beta\gamma^0\gamma^\mu G\sigma^\delta\gamma^0\gamma^\nu], \tag{2.36}$$

which simplifies to

$$\operatorname{Tr}\left[\begin{pmatrix} \mathcal{G}^+_\alpha\mathcal{G}^+_\beta\sigma^\alpha\sigma^x\sigma^\beta\sigma^y & 0 \\ 0 & \mathcal{G}^-_\alpha\mathcal{G}^-_\beta\sigma^\alpha\sigma^x\sigma^\beta\sigma^y \end{pmatrix}\right] = \sum_{a=\pm}\mathcal{G}^a_\alpha\mathcal{G}^a_\beta\operatorname{Tr}[\sigma^\alpha\sigma^x\sigma^\beta\sigma^y] \tag{2.37}$$

after substituting $\mu = x, \nu = y$ and using Eqns. (2.21) and (2.30). Please note that the Latin indices run over the three spatial directions, while the Greek indices run over the four spacetime indices. We would like to find a tangible result for the trace, i.e. an expression containing only Pauli matrices with Latin indices. Then we can use known identities of the Pauli matrices to determine the trace. Writing the trace out explicitly yields

$$\begin{aligned}&\operatorname{Tr}\left[\sigma^\alpha\sigma^x\sigma^\beta\sigma^y\right] = \operatorname{Tr}\left[\left(\delta^\alpha_0\mathbb{I}+\delta^\alpha_k\sigma^k\right)\sigma^x\left(\delta^\beta_0\mathbb{I}+\delta^\beta_k\sigma^k\right)\sigma^y\right] = \\ &\operatorname{Tr}\left[\delta^\alpha_0\delta^\beta_0\sigma^x\sigma^y + \delta^\alpha_0\delta^\beta_k\sigma^x\sigma^k\sigma^y + \delta^\alpha_k\delta^\beta_0\sigma^k\sigma^x\sigma^y + \delta^\alpha_k\delta^\beta_l\sigma^k\sigma^x\sigma^l\sigma^y\right]\end{aligned} \tag{2.38}$$

The anti-commutation relation of the Pauli matrices is $\{\sigma^a,\sigma^b\} = 2\delta_{ab}\mathbb{I}$, which can be used to write the middle two terms in the last line of Eq. (2.38) as

$$\delta^\alpha_0\delta^\beta_k\sigma^x\sigma^k\sigma^y + \delta^\alpha_k\delta^\beta_0\sigma^k\sigma^x\sigma^y = \left(\delta^\alpha_0\delta^\beta_x - \delta^\alpha_k\delta^\beta_0\right)\sigma^x\sigma^k\sigma^y + 2\delta^\alpha_x\delta^\beta_0\sigma^y. \tag{2.39}$$

Now every term in the trace is proportional to Pauli matrices with Latin indices, for which we have the identities

$$\begin{aligned}
&\mathrm{Tr}\left[\sigma^a\right] = 0 \\
&\mathrm{Tr}\left[\sigma^a\sigma^b\right] = 2\delta^{ab} \\
&\mathrm{Tr}\left[\sigma^a\sigma^b\sigma^c\right] = 2i\epsilon_{abc} \\
&\mathrm{Tr}\left[\sigma^a\sigma^b\sigma^c\sigma^d\right] = 2\left(\delta^{ab}\delta^{cd} - \delta^{ac}\delta^{bd} + \delta^{ad}\delta^{bc}\right) \quad .
\end{aligned} \tag{2.40}$$

Applying these identities to Eq. (2.38) yields

$$\begin{aligned}
\mathrm{Tr}\left[\sigma^\alpha\sigma^x\sigma^\beta\sigma^y\right] = {}& 2\delta_0^\alpha\delta_0^\beta\delta^{xy} + 2i\epsilon^{xky}\left(\delta_0^\alpha\delta_k^\beta - \delta_k^\alpha\delta_0^\beta\right) \\
&+2\delta_k^\alpha\delta_l^\beta\left(\delta^{kx}\delta^{ly} - \delta^{kl}\delta^{xy} + \delta^{ky}\delta^{xl}\right)
\end{aligned} \tag{2.41}$$

and because $x \neq y$, we end up with

$$\mathrm{Tr}\left[\sigma^\alpha\sigma^x\sigma^\beta\sigma^y\right] = 2i\left(\delta_z^\alpha\delta_0^\beta - \delta_0^\alpha\delta_z^\beta\right) + 2\left(\delta^{\alpha x}\delta^{\beta y} + \delta^{\alpha y}\delta^{x\beta}\right). \tag{2.42}$$

The contribution of the integral over the terms in the last brackets in Eq. (2.42) is taken to be zero, since the system is rotationally invariant in the xy-plane, so the expression for the polarization diagram becomes

$$\Pi^{xy}(q) = 2ie^2\int\frac{d^4k}{(2\pi)^4}\sum_{\sigma=\pm}\left(\mathcal{G}_z^\sigma(k)\,\mathcal{G}_0^\sigma(k+q) - \mathcal{G}_0^\sigma(k)\,\mathcal{G}_z^\sigma(k+q)\right). \tag{2.43}$$

In order to make the integral in Eq. (2.43) well-defined, we express the Green's functions in Matsubara frequencies, i.e. $k \to (i\omega_n, \vec{k})$, $q \to (i\omega_b, \vec{q})$ and we apply

$$\begin{aligned}
\frac{1}{2\pi i}\int_C dk_0 f(k_0,\omega) &= -\frac{1}{\hbar\beta}\sum_{n=-\infty}^{\infty} f(i\omega_n, i\omega_b) \\
&= -\frac{1}{2\pi i}\int_{C+C'} dz f(z, i\omega_b) N_{FD}(z) \quad ,
\end{aligned} \tag{2.44}$$

where $N_{FD}(z)$ is the Fermi-Dirac distribution as defined in Eq. (1.1). The polarization diagram becomes, after plugging in the definitions of the Green's functions,

$$\begin{aligned}
\Pi^{xy}(i\omega_b,\vec{q},\mu_+,\mu_-) = 2e^2\sum_{\sigma=\pm}\sigma\int\frac{d^3\vec{k}}{(2\pi)^4}\int_{C+C'}dz\left(\frac{z-\mu_\sigma}{(z-\mu_\sigma)^2-|k|^2}\times\right. \\
\left.\frac{k_z+q_z}{(z+i\omega_b-\mu_\sigma)^2-|\vec{k}+\vec{q}|^2} - \frac{z+i\omega_b-\mu_\sigma}{(z+i\omega_b-\mu_\sigma)^2-|\vec{k}+\vec{q}|^2}\frac{k_z}{(z-\mu_\sigma)^2-|k|^2}\right)N_{FD}(z).
\end{aligned} \tag{2.45}$$

One should note that a factor i has been picked up because of the Wick rotation.

Let us first evaluate the integral over z for the first term. The term has poles at $z_1 = \mu_\sigma - |\vec{k}|$, $z_2 = \mu_\sigma + |\vec{k}|$, $z_3 = -i\omega_b + \mu_\sigma - |\vec{k}+\vec{q}|$ and

$z_4 = -i\omega_b + \mu_\sigma + |\vec{k}+\vec{q}|$.

$$\begin{aligned}
&\int_{C+C'} dz \frac{z-\mu_\sigma}{\left(z-\mu_\sigma+|\vec{k}|\right)\left(z-\mu_\sigma-|\vec{k}|\right)} \\
&\times \frac{k_z+q_z}{\left(z+i\omega_b-\mu_\sigma+|\vec{k}+\vec{q}|\right)\left(z+i\omega_b-\mu_\sigma-|\vec{k}+\vec{q}|\right)} N_{FD}(z) = \\
2\pi i \sum_{\alpha=\pm} \Bigg(&\frac{(k_z+q_z)\, N_{FD}(\alpha|\vec{k}|+\mu_\sigma)}{2\left(i\omega_b+|\vec{k}+\vec{q}|+\alpha|\vec{k}|\right)\left(i\omega_b-|\vec{k}+\vec{q}|+\alpha|\vec{k}|\right)} \\
&+\alpha \frac{\left(i\omega_b+\alpha|\vec{k}+\vec{q}|\right)(k_z+q_z)\, N_{FD}(-\alpha|\vec{k}+\vec{q}|+\mu_\sigma)}{2|\vec{k}+\vec{q}|\left(i\omega_b+\alpha|\vec{k}+\vec{q}|+|\vec{k}|\right)\left(i\omega_b+\alpha|\vec{k}+\vec{q}|-|\vec{k}|\right)} \Bigg)
\end{aligned} \tag{2.46}$$

Please note that the term $i\omega_b$ falls out of the Fermi-Dirac distributions, because it is a bosonic frequency and the Fermi-Dirac distribution is periodic in those frequencies. Next we shift the integration variable in the last two terms of Eq. (2.46) by shifting $\vec{k} \to \tilde{k} = \vec{k} - \vec{q}$ and we drop the tilde again. The latter is allowed, since both k and $\tilde{k}$ are integration variables. This yields

$$\begin{aligned}
2\pi i \sum_{\alpha=\pm} \Bigg(&\frac{(k_z+q_z)\, N_{FD}(\alpha|\vec{k}|+\mu_\sigma)}{2\left(i\omega_b+|\vec{k}+\vec{q}|+\alpha|\vec{k}|\right)\left(i\omega_b-|\vec{k}+\vec{q}|+\alpha|\vec{k}|\right)} \\
&+\alpha \frac{\left(i\omega_b+\alpha|\vec{k}|\right) k_z N_{FD}(-\alpha|\vec{k}|+\mu_\sigma)}{2|\vec{k}|\left(i\omega_b+|\vec{k}-\vec{q}|+\alpha|\vec{k}|\right)\left(i\omega_b-|\vec{k}-\vec{q}|+\alpha|\vec{k}|\right)} \Bigg)
\end{aligned} \tag{2.47}$$

We shall now split the denominators of the four terms in Eq. (2.47) into partial fractions, obtaining more convenient expressions.

First term

$$\frac{1}{\left(i\omega_b+|\vec{k}+\vec{q}|+\alpha|\vec{k}|\right)\left(i\omega_b-|\vec{k}+\vec{q}|+\alpha|\vec{k}|\right)} = \frac{A}{i\omega_b+|\vec{k}+\vec{q}|+\alpha|\vec{k}|} + \frac{B}{i\omega_b-|\vec{k}+\vec{q}|+\alpha|\vec{k}|} \tag{2.48}$$

We let

$$A = -\frac{1}{2}\frac{1}{|\vec{k}+\vec{q}|}, \quad B = \frac{1}{2}\frac{1}{|\vec{k}+\vec{q}|}. \tag{2.49}$$

Second term

$$\frac{1}{\left(i\omega_b+|\vec{k}-\vec{q}|+\alpha|\vec{k}|\right)\left(i\omega_b-|\vec{k}-\vec{q}|+\alpha|\vec{k}|\right)} = \frac{A}{i\omega_b+|\vec{k}-\vec{q}|+\alpha|\vec{k}|} + \frac{B}{i\omega_b-|\vec{k}-\vec{q}|+\alpha|\vec{k}|} \tag{2.50}$$

$$A = \frac{1}{2}\frac{1}{i\omega_b+\alpha|\vec{k}|}, \quad B = \frac{1}{2}\frac{1}{i\omega_b+\alpha|\vec{k}|} \tag{2.51}$$

Eq. (2.46) can now be written as

$$-\frac{2\pi i}{4} \sum_{\alpha,\beta=\pm} \left(\beta \frac{k_z+q_z}{|\vec{k}+\vec{q}|} \frac{N_{FD}(\alpha|\vec{k}|+\mu_\sigma)}{i\omega_b+\beta|\vec{k}+\vec{q}|+\alpha|\vec{k}|} - \alpha \frac{k_z}{|\vec{k}|} \frac{N_{FD}(-\alpha|\vec{k}|+\mu_\sigma)}{i\omega_b+\beta|\vec{k}-\vec{q}|+\alpha|\vec{k}|} \right). \tag{2.52}$$

We follow through the same steps for the second term in Eq. (2.45). For the sake of brevity we have performed the shift $\vec{k} \to \tilde{k} = \vec{k} - \vec{q}$ implicitly in the terms that contain $|\vec{k}+\vec{q}|$ in the argument of the Fermi-Dirac distribution.

$$
\begin{aligned}
&-\int_{C+C'} dz \frac{z + i\omega_b - \mu_\sigma}{\left(z + i\omega_b - \mu_\sigma + |\vec{k}+\vec{q}|\right)\left(z + i\omega_b - \mu_\sigma - |\vec{k}+\vec{q}|\right)} \\
&\times \frac{k_z}{\left(z - \mu_\sigma + |\vec{k}|\right)\left(z - \mu_\sigma - |\vec{k}|\right)} N_{FD}(z) = \\
-2\pi i \sum_{\alpha=\pm} &\left(\frac{(k_z - q_z)\, N_{FD}(-\alpha|\vec{k}| + \mu_\sigma)}{2\left(i\omega_b + |\vec{k}-\vec{q}| + \alpha|\vec{k}|\right)\left(i\omega_b - |\vec{k}-\vec{q}| + \alpha|\vec{k}|\right)} \right. \\
&\left. + \alpha \frac{\left(i\omega_b + \alpha|\vec{k}|\right) k_z N_{FD}(\alpha|\vec{k}| + \mu_\sigma)}{2|\vec{k}|\left(i\omega_b + |\vec{k}+\vec{q}| + \alpha|\vec{k}|\right)\left(i\omega_b - |\vec{k}+\vec{q}| + \alpha|\vec{k}|\right)} \right)
\end{aligned}
\tag{2.53}
$$

We split the denominators again in partial fractions.
First term

$$
\frac{1}{\left(i\omega_b + |\vec{k}-\vec{q}| + \alpha|\vec{k}|\right)\left(i\omega_b - |\vec{k}-\vec{q}| + \alpha|\vec{k}|\right)} = \frac{A}{i\omega_b + |\vec{k}-\vec{q}| + \alpha|\vec{k}|} + \frac{B}{i\omega_b - |\vec{k}-\vec{q}| + \alpha|\vec{k}|} \tag{2.54}
$$

$$
A = -\frac{1}{2}\frac{1}{|\vec{k}-\vec{q}|}, \quad B = \frac{1}{2}\frac{1}{|\vec{k}-\vec{q}|} \tag{2.55}
$$

Second term

$$
\frac{1}{\left(i\omega_b + |\vec{k}+\vec{q}| + \alpha|\vec{k}|\right)\left(i\omega_b - |\vec{k}+\vec{q}| + \alpha|\vec{k}|\right)} = \frac{A}{i\omega_b + |\vec{k}+\vec{q}| + \alpha|\vec{k}|} + \frac{B}{i\omega_b - |\vec{k}+\vec{q}| + \alpha|\vec{k}|} \tag{2.56}
$$

$$
A = \frac{1}{2}\frac{1}{i\omega_b + \alpha|\vec{k}|}, \quad B = \frac{1}{2}\frac{1}{i\omega_b + \alpha|\vec{k}|} \tag{2.57}
$$

Eq. (2.53) can now be written as

$$
\frac{2\pi i}{4} \sum_{\alpha,\beta=\pm} \left(\beta \frac{k_z - q_z}{|\vec{k}-\vec{q}|} \frac{N_{FD}(-\alpha|\vec{k}| + \mu_\sigma)}{i\omega_b + \beta|\vec{k}-\vec{q}| + \alpha|\vec{k}|} - \alpha \frac{k_z}{|\vec{k}|} \frac{N_{FD}(\alpha|\vec{k}| + \mu_\sigma)}{i\omega_b + \beta|\vec{k}+\vec{q}| + \alpha|\vec{k}|} \right). \tag{2.58}
$$

Combining the results from Eqns. (2.52) and (2.58), the polarization diagram becomes

$$
\begin{aligned}
\Pi^{xy}(i\omega_b, \vec{q}, \mu_+, \mu_-) = -\frac{ie^2}{2} \sum_{\sigma,\alpha,\beta=\pm} \sigma \int \frac{d^3\vec{k}}{(2\pi)^3} &\left(A_{\alpha,\beta}(\vec{k},\vec{q}) \frac{N_{FD}(\alpha|\vec{k}| + \mu_\sigma)}{i\omega_b + \beta|\vec{k}+\vec{q}| + \alpha|\vec{k}|} \right. \\
&\left. - B_{\alpha,\beta}(\vec{k},\vec{q}) \frac{N_{FD}(-\alpha|\vec{k}| + \mu_\sigma)}{i\omega_b + \beta|\vec{k}-\vec{q}| + \alpha|\vec{k}|} \right),
\end{aligned}
\tag{2.59}
$$

where we have defined $A_{\alpha,\beta}(\vec{k},\vec{q}) = \alpha\frac{k_z}{k} + \beta\frac{k_z+q_z}{|\vec{k}+\vec{q}|}$ and $B_{\alpha,\beta}(\vec{k},\vec{q}) = \frac{k_z}{k} + \beta\frac{k_z-q_z}{|\vec{k}-\vec{q}|}$. We manipulate the expression by writing $N_{FD}(-|\vec{k}| + \mu_\sigma) = 1 - N_{FD}(|\vec{k}| - \mu_\sigma)$, such that the $|\vec{k}|$'s in the Fermi-Dirac distribution have the same sign, which will turn out

to be handy later on.

Moreover, there is still a divergence hidden in each of the cones serperately due to the contribution of the Dirac sea. We therefore define

$$\tilde{\Pi}^{xy}(\omega,\vec{q},\mu_+,\mu_-,C)=\Pi^{xy}(\omega,\vec{q},\mu_+,\mu_-)-\Pi^{xy}(\omega,\vec{q},0,0)+C \tag{2.60}$$

as the true contribution of the vacuum polarization diagram, where the integration over the Dirac sea is subtracted. We subtract a divergence that consists of an infinite and a finite part. The choice of the finite part is somewhat arbitrary, which leaves the freedom to add the constant, C, and fit this to experimental results. The subtraction of the divergence results only in a shift $N_{FD}(|\vec{k}|-\mu_\sigma)\to N_{FD}(|\vec{k}|-\mu_\sigma)-N_{FD}(|\vec{k}|)$. Combined with the manipulation of the Fermi-Dirac distribution the cancellation of the divergence is evident, as the term that is not proportional to any Fermi-Dirac distribution will vanish. The expression we shall be working with now becomes

$$\tilde{\Pi}^{\mu\nu}(i\omega_b,\vec{q},\mu_+,\mu_-,C)=-\frac{ie^2}{2}\sum_{\sigma,\alpha,\beta=\pm}\sigma\alpha\int\frac{d^3\vec{k}}{(2\pi)^3}\times$$
$$\left(A_{\alpha,\beta}(\vec{k},\vec{q})\frac{N_{FD}(|\vec{k}|+\alpha\mu_\sigma)-N_{FD}(|\vec{k}|)}{i\omega_b+\beta|\vec{k}+\vec{q}|+\alpha|\vec{k}|}+B_{\alpha,\beta}(\vec{k},\vec{q})\frac{N_{FD}(|\vec{k}|-\alpha\mu_\sigma)-N_{FD}(|\vec{k}|)}{i\omega_b+\beta|\vec{k}-\vec{q}|+\alpha|\vec{k}|}\right)+C, \tag{2.61}$$

Now that we have obtained a complete expression for the vacuum polarization diagram, we can simplify the angular integral by rewriting it. In addition, since the system is rotationally invariant, we choose $\vec{q}$ to be in the z-direction, whereas the direction of $\vec{k}$ remains unspecified. From now on we use adapt the convention $|\vec{k}|=k$ and $|\vec{q}|=q$. Using these conventions and taking $\cos\phi=\frac{\vec{k}\cdot\vec{q}}{kq}$, we can define

$$\begin{aligned}\cos\theta_{q,k+q}&=\frac{\vec{q}\cdot(\vec{k}+\vec{q})}{q|\vec{k}+\vec{q}|}=\frac{k_z+q_z}{|\vec{k}+\vec{q}|}=\frac{k\cos\phi+q}{|\vec{k}+\vec{q}|}\\ \cos\theta_{q,k-q}&=\frac{\vec{q}\cdot(\vec{k}-\vec{q})}{q|\vec{k}-\vec{q}|}=\frac{k_z-q_z}{|\vec{k}-\vec{q}|}=\frac{k\cos\phi-q}{|\vec{k}-\vec{q}|}\end{aligned}\quad. \tag{2.62}$$

Also, let

$$\begin{aligned}k'&=|\vec{k}+\vec{q}|=\sqrt{k^2+q^2+2qk\cos\phi}\\ k''&=|\vec{k}-\vec{q}|=\sqrt{k^2+q^2-2qk\cos\phi},\end{aligned} \tag{2.63}$$

so that

$$\cos\phi=\frac{k'^2-k^2-q^2}{2kq},\quad \cos\phi=\frac{k''^2-k^2-q^2}{-2kq} \tag{2.64}$$

and we obtain

$$\begin{aligned}\frac{k_z}{|\vec{k}|}+\sigma\frac{k_z+q_z}{|\vec{k}+\vec{q}|}&=\frac{k'^2-k^2-q^2}{2kq}+\sigma\frac{k'^2-k^2+q^2}{2k'q}\\ \frac{k_z}{|\vec{k}|}+\sigma\frac{k_z-q_z}{|\vec{k}-\vec{q}|}&=-\left(\frac{k''^2-k^2-q^2}{2kq}+\sigma\frac{k''^2-k^2+q^2}{2k''q}\right).\end{aligned} \tag{2.65}$$

The integration variables change as

$$\begin{aligned}\sin\phi d\phi &= -\frac{k'dk'}{kq}, \quad \text{with} \quad k' \in [|k+q|, |k-q|] \quad \text{and} \\ \sin\phi d\phi &= \frac{k''dk''}{kq} \quad \text{with} \quad k'' \in [|k-q|, |k+q|].\end{aligned} \tag{2.66}$$

We recognize the terms from Eq. (2.65) in Eq. (2.61) and after substituting them, along with the integration variable, we obtain the simpler form

$$\begin{aligned}&\tilde{\Pi}^{xy}(i\omega_b, \vec{q}, \mu_+, \mu_-, C) = \\ &\frac{-ie^2}{4(2\pi)^2 q}\sum_{\sigma=\pm}\sigma\int_0^\infty dk\int_{|k-q|}^{k+q}dk'\left[\frac{k'(k'^2-k^2-q^2)+k(k'^2-k^2+q^2)}{i\omega_b+k'+k}\right. \\ &-\frac{k'(k'^2-k^2-q^2)+k(k'^2-k^2+q^2)}{i\omega_b-k'-k} - \frac{k'(k'^2-k^2-q^2)-k(k'^2-k^2+q^2)}{i\omega_b+k'-k} \\ &\left.+\frac{k'(k'^2-k^2-q^2)-k(k'^2-k^2+q^2)}{i\omega_b-k'+k}\right]\left(N_{FD}\left(k+\mu_\sigma\right)-N_{FD}\left(k-\mu_\sigma\right)\right)+C,\end{aligned} \tag{2.67}$$

where the trivial integration over the angle θ has been performed implicitly. Since we are working in the limit of zero temperature, the Fermi-Dirac distribution is simplified to

$$N_{FD}(k \pm \mu_\sigma) = \theta(-k \mp \mu_\sigma), \tag{2.68}$$

where $\theta(x)$ is the Heaviside step function. We change the bosonic frequency back to a real frequency, but we add a small, positive imaginary part to the frequency in order to make the integral well-defined, such that $\omega^+ = \omega + i\epsilon$. At the end of the calculation we take the limit $\epsilon \to 0$. Also, let us write out the whole expression again, which is convenient to evaluate the integrals. We are left with

$$\begin{aligned}&\tilde{\Pi}^{xy}(\omega^+, \vec{q}, \mu_+, \mu_-, C) = \\ &\frac{-ie^2}{4(2\pi)^2 q}\sum_{\sigma=\pm}\sigma\int_0^\infty dk\int_{|k-q|}^{k+q}dk'\left[\frac{k'(k'^2-k^2-q^2)+k(k'^2-k^2+q^2)}{\omega^++k'+k}\right. \\ &-\frac{k'(k'^2-k^2-q^2)+k(k'^2-k^2+q^2)}{\omega^+-k'-k} - \frac{k'(k'^2-k^2-q^2)-k(k'^2-k^2+q^2)}{\omega^++k'-k} \\ &\left.+\frac{k'(k'^2-k^2-q^2)-k(k'^2-k^2+q^2)}{\omega^+-k'+k}\right]\left(\theta\left(-k-\mu_\sigma\right)-\theta\left(-k+\mu_\sigma\right)\right)+C.\end{aligned} \tag{2.69}$$

For the evaluation of the k'-integral we use the standard integrals

$$\begin{aligned}\int dx\frac{1}{\pm x+a} &= \pm\log[\pm x+a] \\ \int dx\frac{x}{\pm x+a} &= \pm x - a\log[\pm x+a] \\ \int dx\frac{x^2}{\pm x+a} &= \pm\frac{1}{2}x^2 - ax \pm a^2\log[\pm x+a] \\ \int dx\frac{x^3}{\pm x+a} &= \pm\frac{1}{3}x^3 - \frac{1}{2}ax^2 \pm a^2x - a^3\log[\pm x+a]\end{aligned} \tag{2.70}$$

The integral over k' yields

$$\begin{aligned}
&\tilde{\Pi}^{xy}(\omega^+,\vec{q},\mu_+,\mu_-,C) = \\
&\frac{-ie^2}{4\left(2\pi\right)^2 q^2}\left(\omega^+ - q^2\right)\sum_{\sigma=\pm}\sigma\,\mathrm{sgn}(\mu_\sigma)\int_0^{|\mu_\sigma|} dk\left[\left(2k+\omega^+\right)\left(\log\left[\omega^+ + 2k + q\right] + \log\left[\omega^+ - q\right]\right.\right. \\
&\left. - \log\left[\omega^+ + |k-q| + k\right] - \log\left[\omega^+ - |k-q| + k\right]\right) \\
&+ \left(2k-\omega^+\right)\left(\log\left[\omega^+ - 2k - q\right] + \log\left[\omega^+ + q\right]\right. \\
&\left.\left. - \log\left[\omega^+ - |k-q| - k\right] - \log\left[\omega^+ + |k-q| - k\right]\right)\right] + C.
\end{aligned} \tag{2.71}$$

The integrand for $k < q$ is identical to when $k > q$, hence we can simplify the integral to

$$\begin{aligned}
&\tilde{\Pi}^{xy}(\omega^+,\vec{q},\mu_+,\mu_-,C) = \frac{-ie^2}{4\left(2\pi\right)^2 q^2}\left({\omega^+}^2 - q^2\right)\sum_{\sigma=\pm}\sigma\,\mathrm{sgn}(\mu_\sigma)\int_0^{|\mu_\sigma|} dk\times \\
&\left[\left(2k+\omega^+\right)\left(\log\left[\omega^+ + 2k + q\right] - \log\left[\omega^+ + 2k - q\right]\right.\right. \\
&\left. + \log\left[\omega^+ - q\right] - \log\left[\omega^+ + q\right]\right) \\
&+ \left(2k-\omega^+\right)\left(\log\left[\omega^+ - 2k - q\right] - \log\left[\omega^+ - 2k + q\right]\right. \\
&\left.\left. + \log\left[\omega^+ + q\right] - \log\left[\omega^+ - q\right]\right)\right] + C.
\end{aligned} \tag{2.72}$$

For the last integral we use the standard integrals

$$\begin{aligned}
\int dx \log\left[ax+b\right] &= -x + \left(x + \frac{b}{a}\right)\log\left[ax+b\right] \\
\int dx x \log\left[ax+b\right] &= \frac{1}{2}\left[-\frac{x^2}{2} + \frac{bx}{a} + \left(x^2 - \frac{b^2}{a^2}\right)\log\left[ax+b\right]\right].
\end{aligned} \tag{2.73}$$

The evaluation of the integral results in

$$\begin{aligned}
&\tilde{\Pi}^{xy}(\omega^+,\vec{q},\mu_+,\mu_-,C) = \frac{-ie^2}{16\left(2\pi\right)^2 q^2}\left({\omega^+}^2 - q^2\right)\sum_{\sigma=\pm}\sigma\,\mathrm{sgn}(\mu_\sigma)\times \\
&\left\{8|\mu_\sigma|q + \left[\left(2|\mu_\sigma| + \omega^+\right)^2 - q^2\right]\left(\log\left[\omega^+ + 2|\mu_\sigma| + q\right] - \log\left[\omega^+ + 2|\mu_\sigma| - q\right]\right)\right. \\
&+ \left[\left(2|\mu_\sigma| - \omega^+\right)^2 - q^2\right]\left(\log\left[\omega^+ - 2|\mu_\sigma| - q\right] - \log\left[\omega^+ - 2|\mu_\sigma| + q\right]\right) \\
&\left. +8|\mu_\sigma|\omega^+\left(\log\left[\omega^+ - q\right] - \log\left[\omega^+ + q\right]\right)\right\} + C.
\end{aligned} \tag{2.74}$$

2.3.1 Static and Uniform Limit

Now we can evaluate the CME conductivity in the static limit and in the uniform limit, by evaluating Eq. (2.33). However, one should note that taking the limit $\epsilon \to 0$ causes trouble whenever the real part of the argument of a logarithm is negative. This is dealt with by using

$$\lim_{\epsilon\to 0}\log\left[-x + i\epsilon\right] = i\pi + \log\left[x\right]. \tag{2.75}$$

When taking the limit $q \to 0$, we will encounter the limit

$$\lim_{a\to 0}\frac{1}{a}\left(\log\left[x+a\right] - \log\left[x-a\right]\right) = \frac{2}{x}. \tag{2.76}$$

The static limit is defined by taking the limit $\omega \to 0$ and subsequently $q \to 0$ of the CME conductivity. As was mentioned before this corresponds tow a system with a time-independent applied magnetic field that has small spatial fluctuations with an amplitude that tends to zero. Making the argument of the logarithms positive, Eq. (2.74) can be written for $\omega < q$ as

$$\begin{aligned}
&\tilde{\Pi}^{xy}(\omega^+, \vec{q}, \mu_+, \mu_-, C) = \frac{-ie^2}{8\,(2\pi)^2\, q^2}\left(\omega^{+2} - q^2\right) \sum_{\sigma=\pm} \sigma\, \mathrm{sgn}(\mu_\sigma) \times \\
&\Big\{ 8|\mu_\sigma| q + \left[\left(2|\mu_\sigma| + \omega^+\right)^2 - q^2\right] \left(\log\left[\omega^+ + 2|\mu_\sigma| + q\right] - \log\left[\omega^+ + 2|\mu_\sigma| - q\right]\right) \\
&+ \left[\left(2|\mu_\sigma| - \omega^+\right)^2 - q^2\right] \left(\log\left[-\omega^+ + 2|\mu_\sigma| + q\right] - \log\left[-\omega^+ + 2|\mu_\sigma| - q\right]\right) \\
&+ 8|\mu_\sigma|\omega^+ \left(i\pi + \log\left[-\omega^+ + q\right] - \log\left[\omega^+ + q\right]\right)\Big\} + C.
\end{aligned} \tag{2.77}$$

The CME conductivity in the static limit is

$$\begin{aligned}
&\lim_{q\to 0}\lim_{\omega\to 0} \sigma^x_{CME}(\omega^+, \vec{q}, \mu_+, \mu_-, C) = \lim_{q\to 0} \frac{-e^2}{32\pi^2} \sum_{\sigma=\pm} \sigma\, \mathrm{sgn}(\mu_\sigma)\, \{8|\mu_\sigma| \\
&+ \frac{4|\mu_\sigma|^2 - q^2}{q} \left(\log\left[2|\mu_\sigma| + q\right] - \log\left[2|\mu_\sigma| - q\right]\right) \\
&+ \frac{4|\mu_\sigma|^2 - q^2}{q} \left(\log\left[2|\mu_\sigma| + q\right] - \log\left[2|\mu_\sigma| - q\right]\right)\Big\} + \frac{iC}{q} \\
&= \frac{-e^2}{4\pi^2} \sum_{\sigma=\pm} \sigma\mu_\sigma + \frac{iC}{q}.
\end{aligned} \tag{2.78}$$

If we take a moment to interpret this result, we find something odd. We are considering a system with broken inversion symmetry, such that the two cones are seperated in energy by an amount ΔE. The effective chemical potential of both cones lies on the same energy. If we then turn off the time-dependence in the system, it should be in an equilibrium. If we find a nonzero conductivity, an electric current runs through the system, from which one can extract energy. However, a system in equilibrium must be in a state of lowest energy, so this is clearly a contradiction. We thus conclude that the conductivity in the static limit in equilibrium must be zero and

$$C = \frac{-ie^2 q}{4\pi^2} \sum_{\sigma=\pm} \sigma\mu_\sigma = \frac{-ie^2 q}{4\pi^2} \Delta E. \tag{2.79}$$

We thus claim that in equilibrium

$$\lim_{q\to 0}\lim_{\omega\to 0} \sigma^x_{CME}\left(\omega^+, \vec{q}, \mu_+, \mu_-\right) = 0. \tag{2.80}$$

Now that the constant C has been determined, we can write down a universal expression for the conductivity for any seperation in energy. This reads

$$\begin{aligned}\sigma^x_{CME}(\omega^+,\vec{q},\mu_+,\mu_-,\Delta E) &= \frac{e^2}{8\,(2\pi)^2\,q^3}\left(\omega^{+2}-q^2\right)\sum_{\sigma=\pm}\sigma\,\mathrm{sgn}(\mu_\sigma)\times\\ &\Big\{8|\mu_\sigma|q+\left[\left(2|\mu_\sigma|+\omega^+\right)^2-q^2\right]\left(\log\left[\omega^++2|\mu_\sigma|+q\right]-\log\left[\omega^++2|\mu_\sigma|-q\right]\right)\\ &+\left[\left(2|\mu_\sigma|-\omega^+\right)^2-q^2\right]\left(\log\left[-\omega^++2|\mu_\sigma|+q\right]-\log\left[-\omega^++2|\mu_\sigma|-q\right]\right)\\ &+8|\mu_\sigma|\omega^+\left(i\pi+\log\left[-\omega^++q\right]-\log\left[\omega^++q\right]\right)\Big\}+\frac{e^2}{4\pi^2}\Delta E.\end{aligned} \tag{2.81}$$

This is the central result in this thesis. Now the general expression for the static limit is

$$\lim_{q\to0}\lim_{\omega\to0}\sigma^x_{CME}(\omega^+,\vec{q},\mu_+,\mu_-,\Delta E)=\frac{-e^2}{4\pi^2}\left(\sum_{\sigma=\pm}\sigma\mu_\sigma-\Delta E\right). \tag{2.82}$$

The uniform limit is defined by taking the limit $q\to0$ followed by $\omega\to0$. This corresponds to a system with an applied magnetic field that is completely homogeneous, but has small fluctuations in time with an amplitude that tends to zero. For $q<\omega$ we write Eq. (2.74) as

$$\begin{aligned}\tilde{\Pi}^{xy}(\omega^+,\vec{q},\mu_+,\mu_-,\Delta E) &= \frac{-ie^2}{16\,(2\pi)^2\,q^2}\left(\omega^{+2}-q^2\right)\sum_{\sigma=\pm}\sigma\,\mathrm{sgn}(\mu_\sigma)\times\\ &\Big\{8|\mu_\sigma|q+\left[\left(2|\mu_\sigma|+\omega^+\right)^2-q^2\right]\left(\log\left[\omega^++2|\mu_\sigma|+q\right]-\log\left[\omega^++2|\mu_\sigma|-q\right]\right)\\ &+\left[\left(2|\mu_\sigma|-\omega^+\right)^2-q^2\right]\left(\log\left[-\omega^++2|\mu_\sigma|+q\right]-\log\left[-\omega^++2|\mu_\sigma|-q\right]\right)\\ &+8|\mu_\sigma|\omega^+\left(\log\left[\omega^+-q\right]-\log\left[\omega^++q\right]\right)\Big\}-\frac{ie^2q}{4\pi^2}\Delta E\end{aligned} \tag{2.83}$$

To compute the CME conductivity in the uniform limit, we need to Taylor expand the function up to second order to find

$$\begin{aligned}\lim_{\omega\to0}\lim_{q\to0}\sigma^x_{CME}(\omega^+,\vec{q},\Delta E) &= \lim_{\omega\to0}\frac{-e^2}{64\pi^2}\sum_{\sigma=\pm}\frac{64(|\mu_\sigma|)^3\sigma\,\mathrm{sgn}(\mu_\sigma)}{3\left((2|\mu_\sigma|-\omega)\,(2|\mu_\sigma|+\omega)\right)}\\ &+\frac{e^2}{4\pi^2}\Delta E=\frac{-e^2}{12\pi^2}\sum_{\sigma=\pm}\sigma\mu_\sigma+\frac{e^2}{4\pi^2}\Delta E.\end{aligned} \tag{2.84}$$

The expressions found in the uniform and static limit are in accordance with the literature, such as Ref. [22]. In order to present the results graphically in the next chapter, we would like to express Eq. (2.81) in a different set of variables, i.e. $x=\frac{\omega}{q}$,

$y_\pm = \frac{\mu_\pm}{q}$ and $\mu_\pm$. We also shorten the expression by writing

$$\begin{aligned}\sigma^x_{CME}\left(x, y_+, y_-, \mu_+, \mu_-, \Delta E\right) &= \sum_{\sigma=\pm} \frac{e^2\mu_\sigma}{(2\pi)^2}\sigma\left(x^2-1\right) \\ &\times \left(1 - \sum_{\alpha,\alpha'=\pm} \frac{\alpha}{16|y_\sigma|}\left[\left(2|y_\sigma| + \alpha' x\right)^2 - 1\right]\log\left(\frac{\alpha' x + 2|y_\sigma| - \alpha}{\alpha' x - \alpha}\right)\right) \\ &+ \frac{e^2}{4\pi^2}\Delta E.\end{aligned} \tag{2.85}$$

This can be put in the form

$$\sigma^x_{CME}\left(\omega, q\mu_+, \mu_-, \Delta E\right) = \frac{e^2}{4\pi^2}\left(\sum_{\sigma=\pm}\sigma\mu_\sigma f(\omega/q, \mu_\sigma) + \Delta E\right), \tag{2.86}$$

where $f(\omega/q, \mu_\sigma)$ captures the structure of the dependence of the conductivity on the frequency and momentum. The full expression for the CME conductivity coincides with expressions found in the literature, such as Ref. [23].

Chapter 3

Results

3.1 Results

In this section we investigate the properties of the obtained formula for the CME conductivity by plotting Eq. (2.81) for different choices of parameters in the case $\Delta E = \sum_{\sigma=\pm} \sigma\mu_\sigma$. We are mostly interested in its behaviour as a function of ω/q, for various values of μ_+, μ_- and q.

We will first take a look at the typical behaviour of the function for an arbitrary set of parameters. In Fig. 3.1 the real and imaginary part of the CME conductivity are plotted for $\mu_+ = 15$, $\mu_- = -10$ and $q = 2$. The real part is the conductivity for an applied alternating magnetic field, while the imaginary part is the conductivity when a constant magnetic field is applied. The real part of the conductivity is caused by the imaginary part of the vacuum polarization diagram, which amounts to the self-energy of the photons. This is visualized by the emission and absorption of virtual photons at all energies. The imaginary part of the conductivity is caused by the real part of the vacuum polarization diagram. This contributes only when the electron that emits or absorbs a physical photon is restricted to the Weyl cone. This can be seen in the behaviour of the graphs. The imaginary part of the conductivity is zero in the biggest part of the graph, because for those ω and q absorption and emission of photons is not allowed. It is nonzero for $\omega < q$ and $2\mu_\sigma - q < \omega < 2\mu_\sigma + q$ for $\sigma = \pm$. The last two regions have a width $2q$ because the direction of the momentum can be altered in a transition, making it possible for an electrons to emit or absorb a photon in this region without leaving the cone. The real part of the conductivity does not have these prohibited regions, since it is caused by the emission and absorption of virtual photons, which is not restricted by the Weyl cone.

It is immediately clear that there are three interesting regions where the real and imaginary part undergo a more rapid change than outside these regions. These regions are centered around the vertical lines that are located at $\omega = q$, $\omega = 2\mu+$ and $\omega = 2\mu_-$. The first of these regions is a result of both the electrons with positive and negative chirality, while the second and last are contributions of only the latter and the former, respectively. These regions exhibit typical resonance behaviour, which is caused by interband transitions in both cones. The second peak is higher than the first, because the conductivity has a prefactor, containing an $(\omega/q)^2$, as can be seen in Eq. (2.85). The real part of the conductivity exhibits a local extremum when $\omega = q$. The real part also has two minima and maxima around the second and last vertical line, due to resonance. After the last resonance the real part relaxes to a certain value. The imaginary part has a small bump for $0 < \omega/q < 1$, after which it becomes zero until it reaches the two resonances.

In Fig. 3.2 we show the CME conductivity for all the possible combinations of the signs of the chemical potentials of the cones when $q = 3$. First of all one can see that the resonances lie closer to each other in these graphs, when compared to Fig. 3.1,

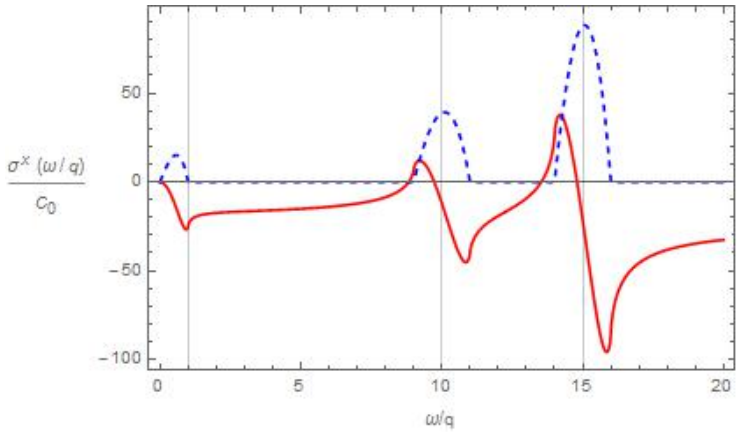

FIGURE 3.1: Real(red, solid) and imaginary(blue, dashed) part of the CME conductivity as a function of ω/q with $\mu_+ = 15$, $\mu_- = -10$, $q = 2$ and $\Delta = \sum_{\sigma=\pm} \sigma\mu_\sigma$. The conductivity is normalized by a factor $C_0 = \frac{e^2}{4\pi^2}$. The vertical lines are positioned at $\omega/q = 1$, $\omega/q = 10$ and $\omega/q = 15$.

due to the different choice of q. The peaks in the real part overlap a bit and choosing a greater q will result in even more overlap. In the Fig. 3.2a and 3.2b the effective chemical potentials are of the same sign and opposite in Fig. 3.2c and 3.2d. It is immediately clear that both the real and imaginary part flip vertically when the sign of an effective chemical potential is changed at the corresponding resonance frequency. We see that the sign of the biggest effective chemical potential determines the sign of the assymptotic value of the conductivity. Furthermore we see that the amplitude of the peak for $0 < \omega/q < 1$ depends on the relative sign of the two effective chemical potentials. The amplitude is biggest when the chemical potentials have a relative minus sign, as the contributions from both cones amplify each other, while they partially cancel each other out when the signs are the same.

It is also interesting to investigate the behaviour of the static and uniform limits of the conductivity. In order to do so, we use the form of Eq. (2.86). To simplify matters we set $\mu_+ = -\mu- = \mu_5$ and we investigate the behaviour of the funtion $f(\omega/q, \mu_5)$. This is also the case in the experiment that is discussed in this thesis. We choose the numerical value $\mu_5 = 50$. This is arbitrarily chosen, since there is no obvious preference. This is plotted in Fig. 3.3. In this plot we see that function $f(\omega/q, 50)$, and therefore also the conductivity, does not depend on ω and q seperately, but is depends on their ratio. $\omega/q \ll 1$ corresponds to the static limit, while $\omega/q \gg 1$ corresponds to the uniform limit. It is now clear that the conductivity is drastically different in both limits. We can now look back at the experiment that has been discussed in the introduction. The team had applied a time-independent, homogeneous magnetic field on the material. In this case the ratio ω/q is not well-defined. The real value can vary over the whole range of the positive numbers. Any perturbation, however small, in either the time-dependent behaviour or the homogeneity of the magnetic field during the experiment could have determined the limit the team was working in. Since the limit in which the experiment was performed is not well-defined, the authors' claim in the paper that they looked at the static case is not necessarily true. To investigate the limit used in the experiment further, the exact value of μ_5 in Eq. (1.21) can be calculated, after which the prefactor in Eq. (2.1) is determined from the given data. However, the values of the parameters in equation μ_5 should be precisely determined before this can be done.

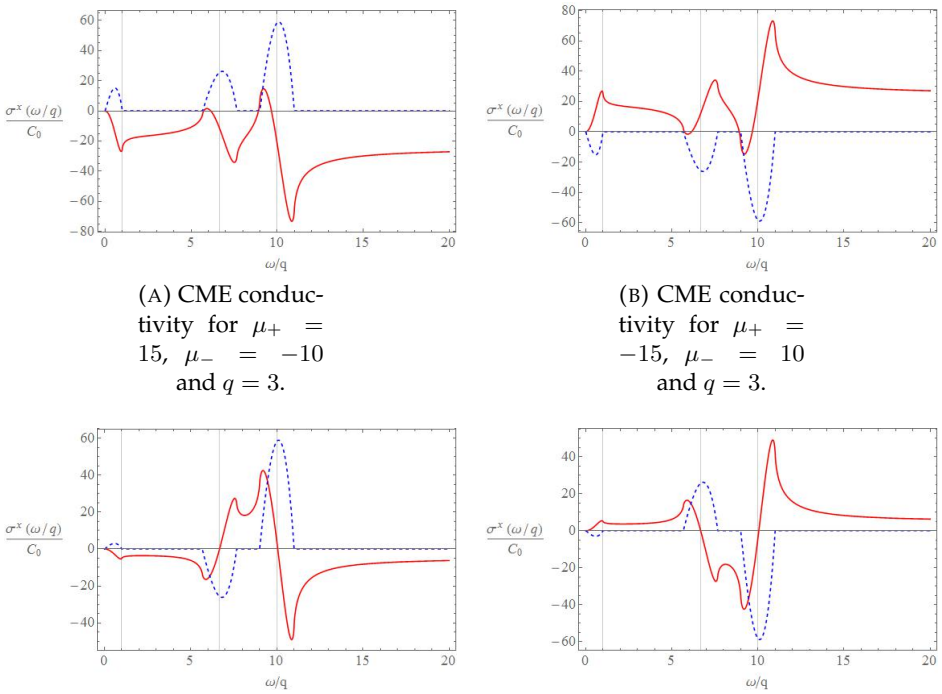

(A) CME conductivity for $\mu_+ = 15$, $\mu_- = -10$ and $q = 3$.

(B) CME conductivity for $\mu_+ = -15$, $\mu_- = 10$ and $q = 3$.

(C) CME conductivity for $\mu_+ = 15$, $\mu_- = 10$ and $q = 3$.

(D) CME conductivity for $\mu_+ = -15$, $\mu_- = -10$ and $q = 3$.

FIGURE 3.2: Real(red, solid) and imaginary(blue, dashed) part of the CME conductivity as a function of ω/q for $\Delta = \sum_\sigma \sigma\mu_\sigma$. The conductivity is normalized by a factor $C_0 = \frac{e^2}{4\pi^2}$. The vertical lines are positioned at $\omega/q = 1$, $\omega/q = \frac{20}{3}$ and $\omega/q = 15$.

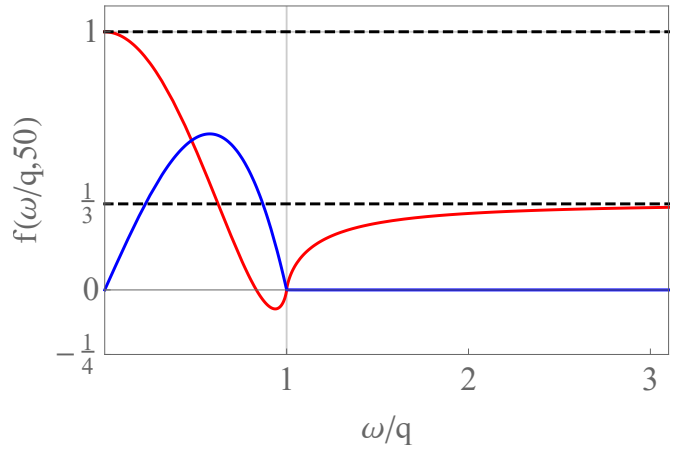

FIGURE 3.3: Plot of the function $f(\omega/q, 50)$ as function of ω/q for $\Delta = \sum_\sigma \sigma\mu_\sigma$. The function is equal to 1 in the static limit, while it is $1/3$ in the uniform limit.

Naively, one would claim that the experiment was not conducted in the static limit, because we have argued in Section 2.3 that there should be no current in the static limit in equilibirum. However, looking back at Eq. (2.81), we find that the choice of ΔE might be different than ours in the experiment. This is indeed the case, since the material used in the experiment is not inherently a Weyl semimetal. It is a

TABLE 3.1: CME conductivity in the static and uniform limit in the case of both effective chemical potential on the same energy and both Weyl points at the same energy in the first and second column, respectively.

	$\Delta E = \sum_{\sigma=\pm} \sigma\mu_\sigma$	$\Delta E = 0$
Static limit	0	$\frac{-e^2}{4\pi^2} \sum_{\sigma=\pm} \sigma\mu_\sigma$
Uniform limit	$\frac{e^2}{6\pi^2} \sum_{\sigma=\pm} \sigma\mu_\sigma$	$\frac{-e^2}{12\pi^2} \sum_{\sigma=\pm} \sigma\mu_\sigma$

Dirac semimetal, but the Dirac fermions were turned into Weyl fermions by applying a magnetic field and therefore breaking time reversal symmetry. In this case the Weyl points lie on the same energy and $\Delta E = 0$. In this case the CME conductivity does not vanish, as can be seen from Eq. (2.81). This is not in contradiction with the argument that systems in equilibrium cannot conduct a current, because there is no equilibrium in this case. The effective chemical potentials of the two cones lie on a different energy, which indicates a non-equilibrium state. The chemical imbalance is fueled by the electric and magnetic fields that are applied. Therefore, extracting energy from the current is possible, because the energy is in fact extracted from the applied fields. Summarized, the value of the CME conductivity depends on which symmetry is broken. In table 3.1 we have presented the static and uniform limit for the case that the effective chemical potentials lie on the same energy and for the case that the Weyl points lie on the same energy.

3.2 Discussion and Outlook

A full derivation has been made of the chiral magnetic conductivity in a Weyl semimetal with a chemical and chiral potential at zero temperature when a magnetic field with a certain wavenumber and frequency. We have derived an analytic function for the conductivity due to the chiral magnetic effect using field-theoretical methods and it is in agreement with the literature. It was found that one has to be careful when deriving this result, since the subtraction of the contribution of the Dirac sea yields a result that is determined up to a constant, ΔE. It is argued that no current is allowed to flow in the static. This statement allowed us to determine ΔE. However, an experiment was presented that might have been conducted in the static limit and the researchers observed a current. We came to the conclusion that in this experiment the static limit does not correspond to an equilibrium, because the time reversal symmetry was broken instead of inversion symmetry. This leads to a different value for ΔE. The values for the conductivity in both limits and for breaking of both symmetries was represented in table 3.1. We emphasize the importance of considering which symmetry is broken when conducting an experiment on the chiral magnetic effect.

Furthermore, the authors of the paper on this experiment claimed to have performed the experiment in the static limit. Because the applied magnetic field was both time-independent and uniform, the limit was not well-defined. Small perturbations in the experiment could have caused a shift to the uniform limit in which the experiment is valid. This shows us that in further experiments the limit has to be taken into account and should be made less sensitive to perturbations. This can be done by applying a magnetic field that is either homogeneous and has nonzero frequency or that is time-independent and has nonzero wavenumber.

Before being able to use WSMs in practical applications, we first need to expand our theoretical knowledge of these materials. This thesis has discussed a model for the conductivity due to the chiral magnetic effect at zero temperature and free of interactions between the electrons themselves. Naturally, in practise the model needs to be extended to finite temperatures. In this thesis one can find an expression, Eq. (2.67), for the chiral magnetic conductivity at finite temperature, but in the end result the temperature has been put to zero. Therefore, from this intermediate expression a temperature-dependent answer can easily be extracted, but this is only possible in a numerical manner. It is impossible to find an exactly solvable analytical model for nonzero temperature. However, one can find a model for low temperatures, which has been done in Ref. [23], or one could use numerical methods to describe temperature-dependent behaviour of the conductivity. Furthermore, a model that incorperates the interactions between the electrons is vital. These interactions are strong of nature. This type of physics can be studied using AdS/CFT correspondence, such as in Refs. [24] and [25], in which a way has already been paved into the world of AdS/CFT correspondence for Weyl semimetals.

Bibliography

[1] "Nextnano3." http://www.nextnano.com/nextnano3/tutorial/1Dtutorial_TightBinding_bulk_GaAs_GaP.htm. Accessed: 2016-12-15.

[2] "Topological matter in optical lattices." http://phys.org/news/2011-11-topological-optical-lattices.html. Accessed: 2016-12-15.

[3] K. S. Novoselov, A. K. Geim, S. V. Morozov, D. Jiang, Y. Zhang, S. V. Dubonos, I. V. Grigorieva, and A. A. Firsov, "Electric Field Effect in Atomically Thin Carbon Films," Oct. 2004.

[4] "Advanced quantum mechanics 2." http://oer.physics.manchester.ac.uk/AQM2/Notes/Notes-6.4.html. Accessed: 2016-12-15.

[5] A. H. Castro Neto, F. Guinea, N. M. R. Peres, K. S. Novoselov, and A. K. Geim, "The electronic properties of graphene," *Reviews of Modern Physics*, vol. 81, pp. 109–162, Jan. 2009.

[6] Z. K. Liu, B. Zhou, Y. Zhang, Z. J. Wang, H. M. Weng, D. Prabhakaran, S.-K. Mo, Z. X. Shen, Z. Fang, X. Dai, Z. Hussain, and Y. L. Chen, "Discovery of a three-dimensional topological dirac semimetal, na3bi," *Science*, vol. 343, no. 6173, pp. 864–867, 2014.

[7] "Band structure: Graphene." http://phelafel.technion.ac.il/~tzipora/band_theory.html. Accessed: 2016-12-15.

[8] H.-R. Chang, J. Zhou, S.-X. Wang, W.-Y. Shan, and D. Xiao, "Rkky interaction of magnetic impurities in dirac and weyl semimetals," *Physical Review B*, vol. 92, no. 24, p. 241103, 2015.

[9] G. E. Volovik, *The Universe in a Helium Droplet*. Clarendon Press ; Oxford University Press, May 2003.

[10] C. Zhang, S.-Y. Xu, I. Belopolski, Z. Yuan, Z. Lin, B. Tong, N. Alidoust, C.-C. Lee, S.-M. Huang, H. Lin, M. Neupane, D. S. Sanchez, H. Zheng, G. Bian, J. Wang, C. Zhang, T. Neupert, M. Z. Hasan, and S. Jia, "Observation of the Adler-Bell-Jackiw chiral anomaly in a Weyl semimetal," Mar. 2015.

[11] M. V. Berry, "Quantal Phase Factors Accompanying Adiabatic Changes," *Proceedings of the Royal Society of London. A. Mathematical and Physical Sciences*, vol. 392, pp. 45–57, Mar. 1984.

[12] "The math kid." http://themathkid.tumblr.com/post/7695548549/riemann-surfaces-of-genus-0-1-2-3-by-ethan-hein. Accessed: 2016-12-15.

[13] Q. Li, D. E. Kharzeev, C. Zhang, Y. Huang, I. Pletikosić, A. Fedorov, R. Zhong, J. Schneeloch, G. Gu, and T. Valla, "Chiral magnetic effect in zrte5," *Nature Physics*, 2016.

[14] R. Belmont, "Charge-dependent anisotropic flow studies and the search for the chiral magnetic wave in {ALICE}," *Nuclear Physics A*, vol. 931, pp. 981 – 985, 2014. {QUARK} {MATTER} 2014XXIV {INTERNATIONAL} {CONFERENCE} {ON} {ULTRARELATIVISTIC} NUCLEUS-NUCLEUS {COLLISIONS}.

[15] R. A. Bertlmann, *Anomalies in quantum field theory*, vol. 91. Oxford University Press, 2000.

[16] H. Banerjee, "Chiral anomalies in field theories," *arXiv preprint hep-th/9907162*, 1999.

[17] P. Hosur and X. Qi, "Recent developments in transport phenomena in weyl semimetals," *Comptes Rendus Physique*, vol. 14, no. 9, pp. 857–870, 2013.

[18] Q. Li, D. E. Kharzeev, C. Zhang, Y. Huang, I. Pletikosic, A. Fedorov, R. Zhong, J. Schneeloch, G. Gu, and T. Valla, "Observation of the chiral magnetic effect in zrte5," *arXiv preprint arXiv:1412.6543*, 2014.

[19] K. Fukushima, D. E. Kharzeev, and H. J. Warringa, "Chiral magnetic effect," *Physical Review D*, vol. 78, no. 7, p. 074033, 2008.

[20] "Linear response theory." http://eduardo.physics.illinois.edu/phys582/LRT.pdf. Accessed: 2016-12-15.

[21] D. Valenzuela, S. Hernández-Ortiz, M. Loewe, and A. Raya, "Graphene transparency in weak magnetic fields," *Journal of Physics A: Mathematical and Theoretical*, vol. 48, no. 6, p. 065402, 2015.

[22] J. Ma and D. Pesin, "Chiral magnetic effect and natural optical activity in metals with or without weyl points," *Physical Review B*, vol. 92, no. 23, p. 235205, 2015.

[23] D. E. Kharzeev and H. J. Warringa, "Chiral magnetic conductivity," *Physical Review D*, vol. 80, no. 3, p. 034028, 2009.

[24] U. Gursoy, V. Jacobs, E. Plauschinn, H. Stoof, and S. Vandoren, "Holographic models for undoped weyl semimetals," *arXiv preprint arXiv:1209.2593*, 2012.

[25] V. Vlachodimitropoulos, "A journey through transport phenomena and holographic interactions in weyl semimetals," master, Universiteit Utrecht, October 2015.